Fall 8-15-2012

Caprock Interactions with the Supercritical CO2 and Brine: A Labratory Study of the Effects of Simulated Geological CO2 Sequestration on Shales from the Black Warrior River Basin, Alabama L

Jessica E. Raines

CAPROCK INTERACTIONS WITH SUPERCRITICAL CO_2 AND BRINE: A LABORATORY STUDY OF THE EFFECTS OF SIMULATED GEOLOGICAL CO_2 SEQUESTRATION ON SHALES FROM THE BLACK WARRIOR RIVER BASIN, ALABAMA

by

JESSICA RAINES

Under the Direction of Daniel M. Deocampo

ABSTRACT

A better understanding of the brine-rock- supercritical CO_2 interaction is needed to evaluate the risks of geologic CO_2 sequestration. The geochemical effects of brine and supercritical CO_2 were examined via laboratory modeling of *in situ* conditions on two reservoir caprocks in the Black Warrior River Basin, the Pottsville and Parkwood Formations. The clay fraction was extracted and treated at ~ 100 bar and 363 K (90 °C) over periods of up to 70 hours. Supercritical CO_2 was introduced as dry ice in a pressurized vessel. Samples were observed using XRD, WD-XRF, AA, SEM, and EDS. Clay fractions contained Fe-chlorite, illite, kaolinite, and quartz. Results show the dissolution of illite, CO_2-brine induced cation exchange ok K^+, and the dissolution of silicate minerals. Steady-state K/Si ratios in the fluid suggest quartz re-precipitation. These interactions could adversely affect the long-term storativity of the caprock and point to a need for further study.

INDEX WORDS: Carbon Sequestration, Black Warrior River Basin, Pottsville Formation, Parkwood Formation, XRD, XRF, AA, SEM, EDS, Illite, Smectite , Enhanced Coalbed Methane Recovery

CAPROCK INTERACTIONS WITH SUPERCRITICAL CO2 AND BRINE: A LABORATORY STUDY OF THE EFFECTS OF SIMULATED GEOLOGICAL CO2 SEQUESTRATION ON SHALES FROM THE BLACK WARRIOR RIVER BASIN, ALABAMA

by

JESSICA RAINES

A Thesis Submitted in Partial Fulfillment of the Requirements for the Degree of

Master of Science

in the College of Arts and Sciences

Georgia State University

2012

CAPROCK INTERACTIONS WITH SUPERCRITICAL CO2 AND BRINE: A LABORATORY STUDY OF THE EFFECTS OF SIMULATED GEOLOGICAL CO2 SEQUESTRATION ON SHALES FROM THE BLACK WARRIOR RIVER BASIN, ALABAMA

by

JESSICA RAINES

Committee Chair: Daniel M. Deocampo

Committee: Seth E. Rose

W. Crawford Elliott

Electronic Version Approved:

Office of Graduate Studies

College of Arts and Sciences

Georgia State University

July 2012

DEDICATION

This work is dedicated to my parents, Lynda and Jim Raines. Without your love, guidance and support, I would not have made it this far.

ACKNOWLEDGEMENTS

I would like to acknowledge all those that helped me along the way. I would like to thank Frank Williams, my favorite anthropology professor, for being the first professor to show confidence in my abilities. Your passion directly influenced my educational experience and taught me to love research. To Seth Rose, my first geology professor, you sparked the fire that eventually led me to a Master of Science in Geology, and your classes continue to be the cornerstone of my educational experience. Ken Terrell, without your advice, I would never have pursued geology. Thank you. Dan Deocampo, thank you for your immeasurable patience and time. Your guidance directly influenced the outcome of this document. Crawford Elliott, thank you for pushing me to continue my education and pursue a Master's degree.

I would also like to thank Lester Williams at the USGS Georgia Water Science Center. Your dogged pursuit of knowledge and impeccable work ethic has left a strong impression on me. To Richard Esposito at Southern Company, thank you for the support of my thesis. You helped to turn my research in a better direction and influenced me to produce a thesis that is relevant to the current energy industry. I would also like to thank those students I shared my educational experience with. Whether we were creating storm clouds in our office, staying up till the early morning studying, pondering the wonders of nature, or just blowing off steam, I would like to thank you. I have made lasting friendships with people I truly respect. I would also like to acknowledge John Hull. Your love and support has helped me to push the limits of my abilities and has made my world a brighter, better place.

TABLE OF CONTENTS

ACKNOWLEDGEMENTS ..... **v**

LIST OF EQUATIONS ..... **xii**

1 INTRODUCTION **1**

1.1 Overview **1**

1.2 Carbon Sequestration **6**

1.2.1 Carbon Dioxide ***7***

1.2.2 Carbon Storage ***7***

1.3 Purpose of the Study **8**

1.4 Previous Research **10**

1.5 Geological Setting **13**

1.5.1 Black Warrior Basin ***13***

1.5.1.1 Pottsville Formation *15*

1.5.1.2 Parkwood Formation *15*

1.5.2 Sample Location ***16***

2 EXPERIMENT **17**

2.1 Procedural Overview **17**

2.2 Sample Analysis Methods **18**

2.2.1 Thin Section Preparation ***18***

2.2.2 XRD Analysis ***18***

2.2.3 XRF Analysis *22*

2.2.3.1 XRF Data Treatment *23*

2.2.4 AA Analysis *24*

2.2.5 SEM/EDS Analysis *25*

2.3 Sample Preparation **26**

2.3.1 Clay Preparation *26*

2.3.1.1 Sodium Acetate Wash *26*

2.3.2 Cube Preparation *27*

2.3.3 Batch Reactions *27*

2.3.4 Brine Composition *29*

2.3.5 XRD Sample Preparation *30*

2.3.6 XRF Sample Preparation *30*

2.3.7 AA Sample Preparation *30*

2.3.8 SEM/EDS Sample Preparation *31*

3 RESULTS **31**

3.1 Thin Section **31**

3.1.1 Pottsville Formation *31*

3.1.2 Parkwood Formation *33*

3.2 Whole Rock Mineralogy **34**

3.3 Fluid Chemistry **35**

3.4 Solid Phase Reactions 37

3.4.1 XRD Clay Analysis 37

3.4.1.1 Relative Abundance of Clay Minerals 39

3.4.2 XRF data 41

3.4.3 SEM/EDS 45

4 DISCUSSION 48

4.1 Mineralogy 48

4.2 Fluid Chemistry 48

4.3 Solid Phase Reactions 49

5 Future Work 50

6 CONCLUSIONS 52

REFERENCES 53

APPENDICES 59

Appendix A - Abbreviations 59

Appendix B - Batch Reaction Pressure Calculations 60

Appendix C - Phillips X-Ray Diffractometer Data 61

Comparison of Phillips and PANalytical data 65

Appendix D - PANalytical X-Ray Diffraction Data 68

Appendix E - XRF Results 73

Appendix G - Atomic Absorbance Data 75

LIST OF TABLES

Table 2-1 Treatment of Teflon Cups with CO_2 27

Table 2-2 Brine Composition..... 30

Table 3-1 Si, K Composition of Brine..... 37

Table 3-2 Clay Mineral Structural Compositions 42

LIST OF FIGURES

Figure 1-1 Possible leakage pathways in an abandoned well 4

Figure 1-2 CO_2 Phase Diagram 7

Figure 1-3 Proposed Geologic CO_2 Sequestration Interval - Black Warrior River Basin, Alabama . 9

Figure 1-4 Tectonic setting of the Black Warrior foreland basin. 14

Figure 1-5 Mississippian Stratigraphy of the Black Warrior Basin 16

Figure 1-6 Sample Locations 17

Figure 2-1 Flow diagram of project design. 18

Figure 2-2 X-ray diffraction according to Bragg's Law. 19

Figure 2-3 Characteristic Radiation 20

Figure 2-4 WDXRF Spectrometer 23

Figure 2-5 Anatomy of a SEM 25

Figure 2-6 Example of characteristic scattering 26

Figure 3-1 Pottsville Formation in Cross Polarized Light (100x) 32

Figure 3-2 Pottsville Formation Sedimentary Structures (actual size) 32

Figure 3-3 Parkwood Formation in Cross-polarized Light (100x) 33

Figure 3-4 Parkwood Formation Sedimentary Structures (2x) 33

Figure 3-5 Pottsville Whole Rock XRD Pattern 34

Figure 3-6 Parkwood Whole Rock XRD Pattern 35

Figure 3-7 AA Detection of Silica in Brine 36

Figure 3-8 AA Detection of Potassium in Brine 36

Figure 3-9 Pottsville Clay Peak Comparison with average d-spacing Angstroms 38

Figure 3-10 Parkwood Clay XRD Peak Comparison with Average d-spacing in Angstroms 39

Figure 3-11 Relative Abundance – Fe-Chlorite (001) 40

Figure 3-12 Relative Abundance - Illite (001) 40

Figure 3-13 Relative Abundance - Kaolinite (002) 41

Figure 3-14 Tri-Plot of All Experimental Clay Composition 42

Figure 3-15 Octahedral cation index of clay in relation to time. 43

Figure 3-16 Octahedral Composition Fe/Al 43

Figure 3-17 Fe2O3/Al2O3 vs. Time 44

Figure 3-18 Tetrahedral Composition 44

Figure 3-19 Tetrahedral Composition vs. Time 45

Figure 3-20 SEM image Pottsville Unaltered and EDS 46

Figure 3-21 Pottsville No CO2 and EDS 46

Figure 3-22 SEM Image Pottsville CO2 and EDS 46

Figure 3-23 SEM Image Parkwood Unaltered and EDS 47

Figure 3-24 SEM Image Parkwood No CO2 and EDS 47

Figure 3-25 SEM Image Parkwood CO2 and EDS 47

LIST OF EQUATIONS

Equation 1-1 Carbonic Acid Formation 10

Equation 2-1 Bragg's Law derived. 19

Equation 2-2 Relative Abundance Calculation 21

Equation 2-3 Calculation of structural formula 24

Equation 2-4 Formula to calculate the total volume of clay. 28

Equation 2-5 Ideal Gas Equation 29

1 INTRODUCTION

1.1 Overview

According to the International Panel on Climate Change (IPCC) (2001) there is strong evidence supporting a direct connection between increasing global mean temperatures and human activities over the past five decades. These activities are expected to continue throughout the 21st century, changing the Earth's atmospheric composition by the introduction of a variety of anthropogenic gasses. Carbon dioxide (CO_2) is currently the greatest concern due to the volume being emitted into the atmosphere and its role as a greenhouse gas. Options for the reduction of net atmospheric CO_2 include, but are not limited to, reduction in energy consumption, using fuels that are less carbon intensive, increasing the use of renewable energy sources and/or nuclear power, sequestering CO_2 biologically or in soils, or capturing CO_2 and storing it either physically or chemically (Metz, 2005).

Between 2007 and 2008, global CO_2 emissions dropped 3%, but this is largely related to the most recent economic downturn and higher energy prices and does not reflect the long-term increase in carbon emissions (http://www.eia.gov/oiaf/1605/ggrpt/carbon.html#total). Power generation for electricity remains the principal contributor to total anthropogenic carbon emissions, producing as much CO_2 as all other industries combined. The transportation sector is currently a distant third; however, it is growing faster in rates of emission than any other sector (Metz, 2005). Meeting the United Nations Framework Convention on Climate Change (UNFCCC) carbon goals to stabilize the atmosphere is a challenge that will require not only the reduction of carbon emissions but also improvements to existing technologies designed to control emissions and reduce atmospheric concentrations of CO_2. The extent to which carbon emissions will be reduced will depend on the implementation of policy which penalizes excess emission and incentivizes the reduction or storage of emissions, and these policies will likely drive

the investment necessary to realize the research and innovations that will bring about safer, smarter, and more efficient carbon control technologies.

A main factor in the selection of new technologies aimed at reducing carbon emissions and atmospheric concentration is cost in relation to effectiveness. In the past two decades, the geologic sequestration of CO_2 has shown itself to be a viable carbon mitigation strategy. Harnessing CO_2 for profitable applications is hardly a novel concept. Studies from as early as three decades ago (Horn and Steinberg, 1982) discuss the separation of CO_2 and other gases from natural gas streams for use in industrial processes, and more recently, carbon sequestration has become accepted as a feasible option for industrial emissions control because of its utility in enhanced oil recovery (EOR) and enhanced coalbed methane recovery (ECBM). Even without considering further industrial applications, CO_2 can be stored for the long term in saline formations, basalts, and coal seams. However, without profit return or subsidization, CCS is cost prohibitive.

The oil and gas industry has been using the same technologies needed for the geological sequestration of CO_2 for many years. Drilling, injection, computer simulation of reservoir dynamics, and geotechnical modeling are all procedures and techniques that can be applied to the geological storage of CO_2 (Metz, 2005). The Sleipner field in the North Sea is the oldest well-studied carbons sequestration project currently online (Chadwick *et al.*, 2004). The project has been running since 1996 with CO_2 being injected into the Mio-Pliocene Utsira Sand overlain by the 250 meter thick Nordland Group shales (Gaus *et al.,* 2005). The possibility of enhanced resource extraction and additional Clean Development Mechanism (CDM) credits further incentivize the implementation of carbon capture and storage (CCS) projects as a resource maximizing and overhead reducing strategy.

Costs associated with the geologic sequestration of CO_2 are generally site specific and are dependent upon factors such as reservoir depth, subsurface conditions (such as reservoir thickness and permeability), the construction and maintenance of pipelines to distribute and deliver CO_2, whether the

site is onshore or offshore, the amount of previous research at a potential site, and the actualized return on saleable products. The projected cost of geological sequestration is within the range of 0.2-30.2 US dollars per ton of CO_2 (US$/t CO_2) (Metz, 2005). Without saleable resources post-CO_2 injection, the aggregate cost of geologic sequestration would be significantly higher; however, EOR is expected to create negative storage costs of 10-16 US$/t$CO_2$ for oil prices of 15-20 US$/barrel (Hendricks *et al.*, 2002, Allinson *et al,.* 2003, Bock *et al.,* 2003). However, with current oil prices around 90 US$/barrel, EOR will only offset storage costs.

Geologic storage is a relatively new field and many knowledge gaps still exist. The potential long-term cost of geological storage is known to a degree, but there are few cost reports from capture to monitoring that have been created from experience (Metz, 2005). There is also a need for global storage capacity estimation in order to quantitatively assess the total potential of CO_2 sequestration for the purposes of atmospheric carbon reduction. In regard to the conduct of CO_2 sequestration, reliable modeling of complex hydrogeological, geochemical, and geomechanical processes is necessary for any estimation of storage performance. Also, the kinetics of geochemical trapping and the long-term storativity of the reservoir rock, as well as the process of CO_2 adsorption and CH_4 desorption in coal fields need further exploration.

The reliable modeling of complex hydrogeological-geochemical-geomechanical process is necessary for the estimation of storage performance. There is not currently an accurate method to conduct a total quantitative assessment of the risk to human population health and local environments. The circumstances that create a greater potential for leakage form a major knowledge gap which must be closed before any meaningful risk analysis can be undertaken. Spatial distribution of abandoned wells needs to be fully researched and georeferenced, and methods for detecting and monitoring CO_2 leakage via remote-sensing and surface detection need to be advanced. Along with these advancements, long-term monitoring strategies and networks need to be established. Liability frameworks also need to be

developed to reduce uncertainties about pilot programs, site selection, stewardship, and site decommissioning (Metz, 2005).

For any CO_2 sequestration project, risk is a function of the magnitude of a potential hazard, and the likelihood that the hazard will occur. Leakage is the leading cause of potential hazards. Carbon dioxide existing as a separate phase may escape from formations, fluids, or carbon capture and transport hardware in many ways (Figure 1-1).

Pipeline failure occurs when a hole is put into the line or there is a rupture in the system; however, the record of CO_2 pipelines from 1990 to 2001 shows only 10 accidents without any injuries or fatalities, which corresponds to a frequency of 3.2×10^{-4} incidents per km per year (Gale and Davidson, 2003). Unlike natural gas, CO_2 is denser than air, so it will not quickly disperse from the point of leakage, therefore creating an increased risk of fatality for individuals in the immediate vicinity of the leak. Since the CO_2 is pressurized into liquid form in the pipeline, if there is a rupture, the liquid will freeze before beginning sublimation and moving into the atmosphere. Once injected into a reservoir, the risk of leakage has the potential to decrease, depending on the efficacy of the Monitoring, Managing and Verification (MMV) strategies.

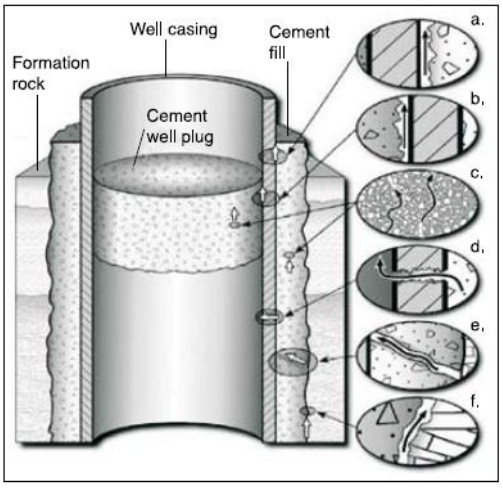

Figure 1-1 Possible leakage pathways in an abandoned well
(a-b) between casing and cement wall plug; (c) through cement plugs; (d) through casing; (e) through cement wall; and (f) between cement wall and rock. (from Gasda *et al.,* 2004)

Geologic storage sites are designed to confine all of the injected CO_2 over geologic time scales; however, because of the lack of current studies on CO_2 leakage and experience with previously engineered systems, the IPCC has called for quantitative estimates based on what evidence there is available (Metz, 2005). Pressure and diffusion will primarily drive the subsurface flow of CO_2. If the pressure of the CO_2 gas is greater than the pore pressure of the caprock, the CO_2 will migrate upwards through the caprock (Metz, 2005). Leaked CO_2 may reach the water table and migrate into the overlying vadose zone. Here, the pore spaces are filled with water and air, and since CO_2 is denser than air, it will displace the air present, leading to potential 100% gas concentrations in the pore volume not filled with water (Oldenburg *et al.*, 2003). The carbon dioxide will continue migrating upwards in this manner until the surface is reached. Similar situations can occur in offshore storage sites, but there the leakage will occur in ocean bottom sediments and then move vertically through the water column.

Carbon dioxide injected into coal seams has the potential to escape through unmapped fractures and cleats. CO_2 in coal also has the potential to be sorbed into the surrounding strata, and if the pressure system of the coal seam is later reduced, there is potential for the CO_2 to desorb from the coal and be released (Pashin, 1991a, Metz, 2005).

Leakage from injection wells, abandoned wells, or poorly sealed wells poses a substantial risk, especially when CO_2 is sequestered in old oil and gas fields. In any given area, the number of these wells can be unknown. Drilling a well not only produces a hole, it also introduces manmade materials into the ground. If an old exploratory well was considered a “dry hole” when it was dug, it is unlikely that the well would have been sealed, as this wasn’t required by regulations in the early days of resource extraction. Leakage could easily occur through this type of well, unbeknownst to those undertaking a sequestration project. Even if an abandoned well is plugged, gasses could still escape through the area between the well casing and the cement wall, the cement plug and the well casing, through a point of weakness in the well casing, through the cement wall, or between the cement wall and the rock (Gasda

et al., 2004). Despite the risk of leakage through abandoned wells, old oil fields may serve as a natural analogue for the ideal sequestration site conditions (Gaus, 2010). This is because they have contained fluids at high pressures effectively for long periods of geologic time.

1.2 Carbon Sequestration

Carbon Capture and Storage (CCS) involves the use of various technologies to collect, concentrate, transport, and store CO_2, with the expressed goal of permanently separating it from the atmosphere. CO_2 can be effectively captured in several different ways. The most typical method involves separating it from a gas stream with techniques like scrubbing the stream with chemical solvents (Siddique, 1990). The reason that gas separation is the most common is because the majority of the research on carbon capture is on the reduction of emissions from a large point source, typically in the energy industry.

Another method of carbon sequestration is by ambient capture. Zeman (2007) has proposed a method that involves a scrubber technology that absorbs CO_2 directly into a sodium hydroxide solution that is then removed from its alkaline carbonate form into lime, or calcium carbonate. Thermal calcination then removes the CO_2 by thermal decomposition (Zeman, 2007). This technology is effective and comparable in energy consumption to gas separation technologies used on coal plants.

The transportation of CO_2 requires the compression of the gas to reduce its volume, and then transport in a liquid state. This technology is not new, as there are already 2500 km of pipelines existing in the western United States that transport 50 $MtCO_2$ per year. These pipelines were originally designed to carry CO_2 from natural sources to old oil fields for enhanced oil recovery in west Texas and other locations similar to this (Metz, 2005).

1.2.1 Carbon Dioxide

At standard pressure and temperature conditions, CO_2 is in a gas state. At low temperatures, CO_2 is a solid (a state commonly known as dry ice). At intermediate temperatures (between -56.5˚C and 31.1˚C), CO_2 can be liquefied under compression. At temperatures above 31.1˚C, CO_2 enters into a supercritical state where it behaves as a gas with a density approaching or exceeding liquid water. In its dense or liquid phase, CO_2 occupies about 0.2% of its original volume of the gas at standard temperature and pressure (STP). This state is ideal for the conveyance of CO_2 through pipelines. Figure 1-2 shows the sublimation point, the triple point and the critical point of CO_2 (Metz, 2005).

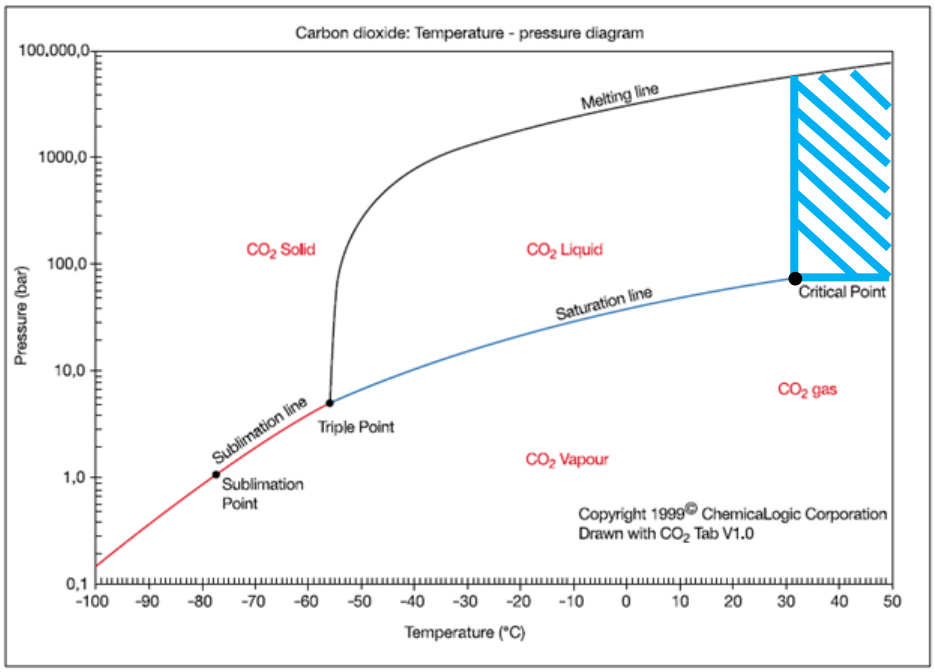

Figure 1-2 CO_2 Phase Diagram
Phase diagram modified from (Metz, 2005) showing the critical point where CO_2 shifts from gas to liquid and then to a supercritical fluid (striped region) at the critical point which is at 31.1˚C and 1,071 psi.

1.2.2 Carbon Storage

There are several methods for the long-term storage of CO_2. Captured CO_2 has the potential to be stored in three different types of media: supercritical storage in deep geological formations, liquid

storage in the ocean, and solid state storage (mineralization) by the reaction of CO_2 with metal oxides to produce more stable carbonates (Aydin, 2010). Of the options, mineral carbonation has a high cost with great environmental risk. Though injection into deep sea water was one of the earliest proposed methods (Marchetti, 1977), ocean storage is still a poorly understood technology and inherently risky (Aydin, 2010). This leaves carbon capture and geologic storage (CCGS) as the most viable alternative. CCGS has several advantages including (1) a long-standing history of prior research and experience gained from oil and gas exploration which lends itself to immediate applications of CCGS technology (2) large potentials for storage capacity worldwide (3) and having the potential for long-term storage on the scale of thousands of years or more.

1.3 Purpose of the Study

There have been very few publications of laboratory experiments attempting to explain the geochemical effects of CO_2 injection into saline formations on reservoir seals (e.g., Almeu *et al.*, 2011). Experimental studies simulating *in situ* pressure and temperature conditions are scant, and there are little data to describe mineral reactions after the injection of CO_2 (e.g., Wigand *et al.*, 2008, Shao *et al.*, 2010, Credoz *et al.*, 2011, Shao *et al.*, 2011a, Almeu *et al.*, 2011). Laboratory results simulating *in situ* reservoir conditions show that during exposure to supercritical CO_2 and brine, the alteration of rock forming minerals occurs. These reactions include the dissolution and precipitation of rock-forming minerals, with a tendency toward dissolution (Almeu *et al., 2011, Liu et al.*, 2012). The purpose of this study is to further the understanding of the interaction of supercritical CO_2, brine and the clay fraction of shaley caprocks by observing the change in clay composition, structure, and brine chemistry. Shales from the Pottsville and Parkwood Formations ((33˚27’28.92”N, 86˚42’56.78”W) and (33˚36’42.44” N, 86˚17’ 14.46”W) respectively) (Figure 1-3) were selected as targets because of proprietary research suggesting the viability of geological CO_2 sequestration in these formations, though at the time of sample selection, the units were not fully characterized. The shales of the Pottsville and Parkwood Formation were suggested to

serve as a regional seal over proven injection zones, making them ideal targets for testing (http://www.netl.doe.gov/publications/proceedings/10/rascp/Alabama_Clark.pdf).

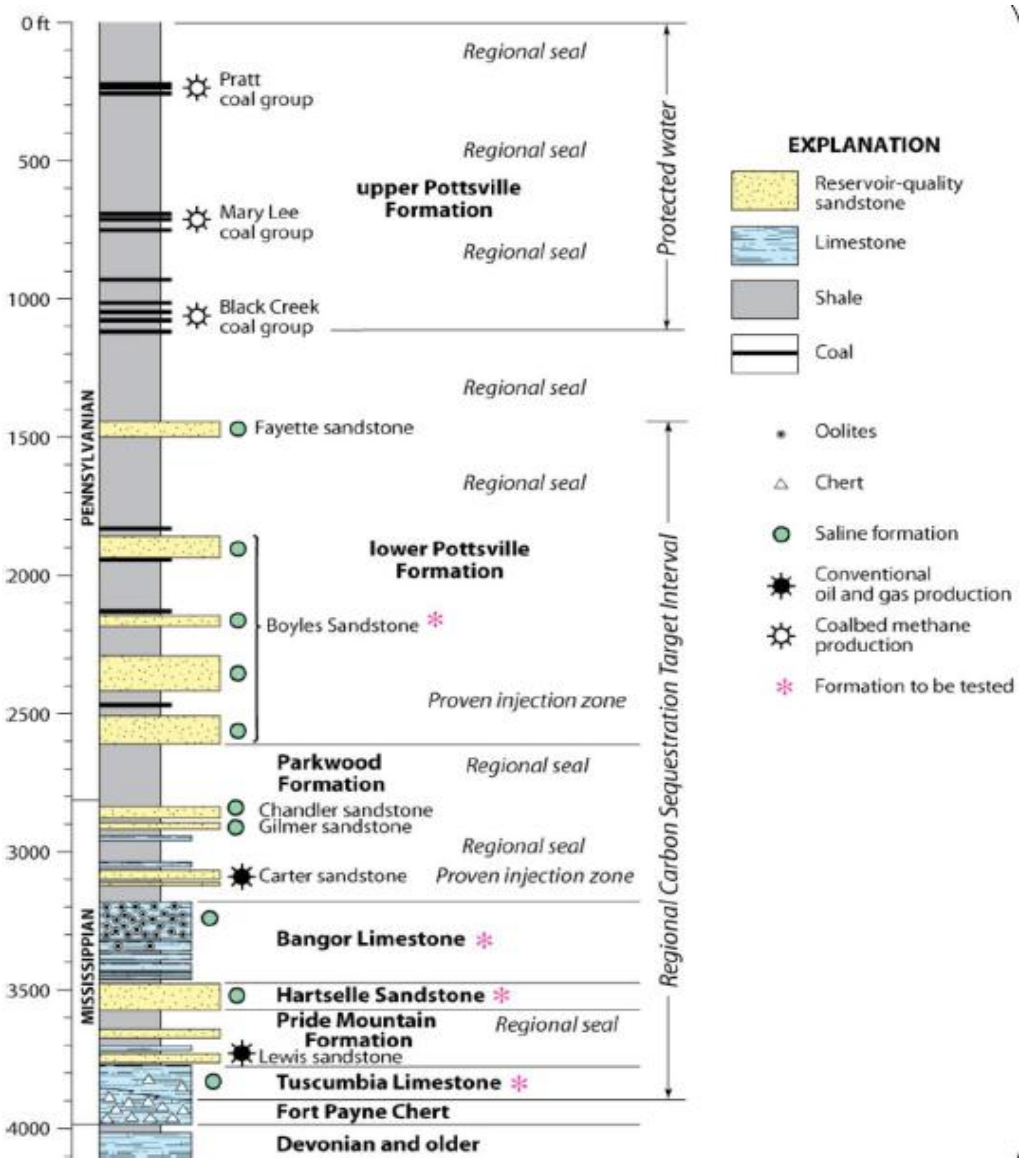

Figure 1-3 Proposed Geologic CO_2 Sequestration Interval - Black Warrior River Basin, Alabama
from: http://www.netl.doe.gov/publications/proceedings/10/rascp/Alabama_Clark.pdf

1.4 Previous Research

Marchetti (1977) was one of the first researchers to propose the mitigation of atmospheric CO2 by injecting it into ocean currents with temperatures between 0-10˚C, which would carry the CO_2 deep into the ocean for more permanent storage. However, this method is inherently risky. When CO_2 in a gas state contacts water, it will dissolve into the water until equilibrium is reached (Drever, 1997). The solubility of CO_2 in water, according to Henry's Law, depends on temperature, the partial pressure of the gas over the liquid, the nature of the water and of the gas (Drever, 1997). The reaction between the dissolved CO_2 and the water produces a weak acid, carbonic acid (H_2CO_3):

$$CO_2 + H_2O = H_2CO_3$$

Equation 1-1 Carbonic Acid Formation

As the amount of carbonic acid in the water increases, the pH of the water will be driven down, becoming more acidic. Natural waters have a pH of about 5-7, but as the acid is introduced, it increases the pCO_2, and the pH can be driven down to 3-4 (Drever, 1997, Deocampo and Ashley, 1999).

These lower pH ranges will have a direct effect on marine ecosystems. No controlled experiments in the deep ocean have been performed. However, it is predicted that ecosystem consequences will increase proportionally to the amount of CO_2 in the system (Metz, 2005). This can lead to natural buffering caused by the release of calcium carbonate ($CaCO_3$) from the shells of marine organisms. The increase in CO_2 composition in the water also can cause an accumulation of CO_2 in marine animals, which can lead to death (Metz, 2005).

The geological sequestration of atmospheric carbon, which has a predicted lower risk of negative environmental effects (Aydin, 2010), has been studied in a variety ways since the 1970's. Within the context of this study, more recent research about the effects of CO_2 on the surrounding geologic formations is the most relevant.

The mixing of CO_2 into reservoir brine has been found to change the brine density and pH over time (Kumar *et al.*, 2008). The same study modeled changes in the water rock interactions and found they occurred rapidly at first but after that, only slower mineral reactions shifted the brine chemistry. This places an emphasis on the need to model the dissolution and precipitation reactions that could significantly alter rock-fluid properties of the reservoir rocks or the caprocks.

Just like with the dissolution of calcium carbonate bearing marine animals, carbonate and sulphate minerals, which are characterized by fast reaction times, will quickly dissolve into the CO_2 saturated brine and will continue to do so until equilibrium is reached and could produce secondary reactions like the precipitation of gypsum (Gaus, 2010). The brine, even after pH buffering from carbonate dissolution, will be strong enough to attack alumino-silicate minerals, which are abundant in sedimentary rocks (Gaus, 2010). Wigand (2008) observed an increased aluminum (Al) and Silica (Si) brine composition in simulated geological sequestration conditions, which confirms the dissolution of aluminosilicates. An example of the alteration of clay minerals where CO_2 becomes trapped in clay was given by Gaus (2010):

$$\underset{\text{Chlorite}}{Fe_{2.5}Mg_{2.5}Al_2Si_3O_{10}(OH)_8} + 2.5\underset{\text{Calcite}}{CaCO_3} + 5CO_2 \leftrightarrow 2.5\underset{\text{Siderite}}{FeCO_3} + 2.5\underset{\text{Dolomite}}{MgCa(CO_3)_2} + \underset{\text{Kaolinite}}{Al_2Si_2O_5(OH)_4} + \underset{\text{Chalcedony}}{SiO_2} + 2H_2O$$

Permanent trapping capacities of rock compositions can be calculated and modeled; however, the results are subject to many uncertainties. Exact brine composition has the potential to affect cation exchange in the reaction. Some experimental models used synthetic brines for the reaction (e.g., Giammar *et al.,* 2005, Liu *et al.*, 2012), some use a sodium chloride (NaCl) solution (e.g., Credoz *et al.*, 2011, Shao *et al.*, 2011a, Almeu *et al.*, 2011, Wigand *et al.*, 2008), and some use deionized H_2O (Shao *et al.*, 2010), but there is no consistent method for modeling brine in laboratory conditions. Reaction kinetics are key to understanding mineral trapping capacity or the impact on matrix permeability during

CO_2 storage. Rapid kinetic reactions, like those of carbonates and some sulphates, can be directly quantified in the laboratory, but slower reactions, like those involving aluminosilicates, are not well known at reservoir conditions (Gaus, 2010) and need to be calculated using a variety of models.

The methods relevant to this research are the ones produced in laboratory settings, exhibiting the effects of brine and CO_2 on minerals at geological sequestration conditions. To understand the effects of salinity on mineral dissolution, Shao *et al.* (2011b) ran a series of experiments on phlogopite ($KMg_3AlSi_3O_{10}(OH)_2$) where brines of various percent composition NaCl were used. It was found that brines of lower salinity more rapidly dissolved phlogopite and in turn formed silica-rich nanoparticles of secondary minerals at higher rates and abundance, and these nanoparticles were predicted to have the capacity to change the physical properties of rocks.

Hu *et al.* (2011) found in reactions with isolated biotite in supercritical CO_2 conditions with brine, biotite dissolution occurred at increasing rates over a 96 hour period. During this reaction time, according to XRD and EDS data, secondary precipitation of fibrous illite and kaolinite occurred. This is important because the formation of fibrous illite has been shown to reduce permeability if hydrocarbon reservoirs (Hu *et al., 2011)* and could severely affect the injection potential of a sequestration site.

Credoz *et al.*, (2011) showed that mixed-layered illite-smectites reacted in the presence of potassium feldspar showed that pH had a direct control on the degree of illitization of the mixed-layer mineral. In this study, it was shown that higher pH induced a 'proton-promoted' illitization process. When pH was lowered, the illitization of the mixed-layered mineral slowed and the reaction was suggested to be more pressure driven.

Dissolution and precipitation in geological CO2 sequestration conditions also occur in shaley caprocks. Dissolution reactions are controlled by the carbonate content of the shale prior to reaction

(Almeu *et al.*, 2011), being that carbonates are more reactive to low pH, high temperature conditions. Common components of shale, illite, smectite, and chlorite, are also shown to dissolve in the laboratory simulations (Almeu *et al., 2011, Liu et al.*, 2012). Mineral precipitations of illite, smectite and carbonates were also common amongst the caprock studies, and were identified by SEM/EDS and XRD.

It is important to emphasize the lack of a common approach. All experiments (e.g., Almeu *et al., 2011,* Credoz *et al.*, 2011, Hu *et al.,* 2011, Shao *et al.*, 2011b, *Liu et al.*, 2012) used different pressures, temperatures, pH ranges, starting brines, and mineral compositions. No common approach to the laboratory analysis of the effects of geological CO_2 sequestration conditions on reservoir rocks or common minerals found in those reservoirs was unveiled in the development of this research. Therefore, though end results might be comparable, the kinetic pathway to that end is not necessarily the same.

1.5 Geological Setting

1.5.1 Black Warrior Basin

The Black Warrior Basin is a foreland basin from the late Paleozoic found in Alabama and Mississippi (Thomas, 1977, Pashin and Gastaldo, 2009). The basin formed during the early stages of the Pangean supercontinent assembly. Its sedimentary fill reflects its tectonic evolution in conjunction with the climatic changes related to drift though the southern tradewind belt into the equatorial zone (Thomas, 1988, Pashin and Gastaldo, 2009). Generally triangular in shape, it is bounded to the southwest by the Ouachita orogeny, to the north by the Nashville Dome, and to the southeast by the Appalachian orogeny (Thomas, 1988) (Figure 1-4).

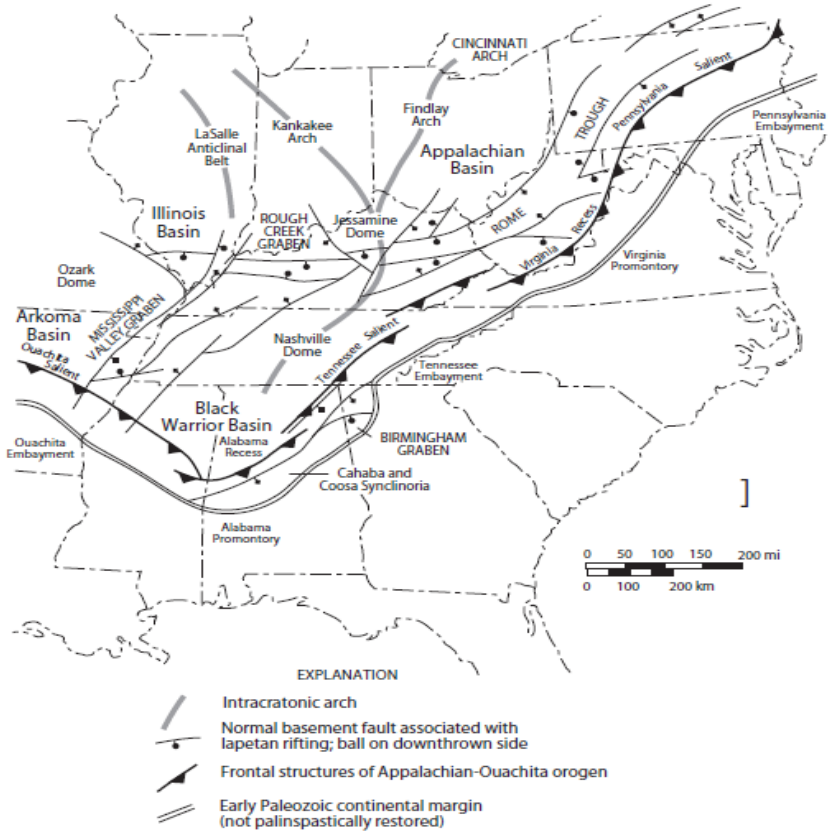

Figure 1-4 Tectonic setting of the Black Warrior foreland basin.
Source: (Thomas, 1988; Pashin and Gastaldo, 2009)

Carboniferous strata are preserved in the Black Warrior Basin and are found in the Appalachian thrust belt as well as in the eastern Black Warrior Basin; however, the rest of the strata are buried under the Mesozoic and Cenozoic fill of the Gulf of Mexico Basin (Pashin and Gastaldo, 2009). The basin is categorized as a southwest-dipping homocline possessing many faults superimposed along the southeastern margin of the homocline of the Appalachian fold and thrust faults (Pashin, 2008). The basin is developed on the Alabama Promontory, which is thought to be an outcropping of the Laurentian continental platform developed during the Early Cambrian Iapetan rifting (Thomas, 1997, Pashin and Gastaldo, 2009). For this study, two units from the Basin have been selected, the Pottsville Formation and the Parkwood Formation.

1.5.1.1 Pottsville Formation

The Pottsville Formation is over 3000 meters thick, and is found in the center of the Black Warrior Basin (Hewitt, 1984), and progressively thins to the north as a product of depositional thinning and post-Pennsylvanian erosion (Demko and Gastaldo, 1992). Early Pennsylvanian subsidence of the Appalachian thrust belt created space for the Pottsville Formation, which is said to be Westphalian A in age (Demko and Gastaldo, 1992). Westpahalian A fell at the beginning of the Pennsylvanian and lasted for about 10 Mya (315-305 Ma).

The upper Pottsville is a siliciclastic succession containing vertically stacked 4th-order parasequences (Pashin, 2004, 2007), meaning sequences that occur less than every one million years. The upper portion of the formation is dominated by coal beds and marginal-marine and non-marine sandstones and shales, while the lower portion is dominated by marine shales (Pashin, 2007).

1.5.1.2 Parkwood Formation

The Parkwood Formation, from the late Mississippian, early Pennsylvanian epoch, is composed primarily of interbedded sandstone and shale, and contains one of the most viable conventional hydrocarbon reservoirs in the Basin. The upper Parkwood is lithologically heterogeneous with gray shale, sandstones, clay and some thin beds of coal with no economic value. The middle Parkwood is dominated by limestone and shale (Pashin, 2007). The Mississippian-Pennsylvanian boundary in the upper Parkwood Formation has not been precisely mapped within the Black Warrior Basin (Pashin, 2007). Figure 1-5 shows the stratigraphy of the Parkwood Formation in the Black Warrior River basin.

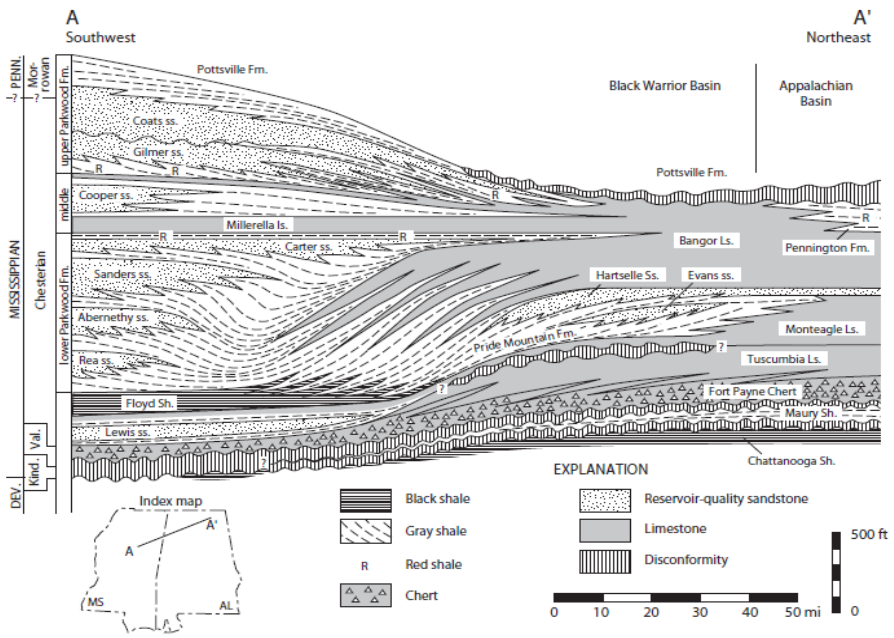

Figure 1-5 Mississippian Stratigraphy of the Black Warrior Basin

Stratigraphic cross section of the Black Warrior basin from northeast Alabama to east-central Mississippi. This section shows the lower Pottsville Formation in contact with the Parkwood Formation. (from Pashin, 1994)

1.5.2 Sample Location

To locate the formations, a digital Alabama Geological Survey map of the state was overlaid onto a Google Maps roadmap and a topography map. Possible locations along major roads were selected and then located. If there was a major road-cut within the latitudinal/longitudinal range of the formation along the roadway, it was selected. 'Clean' samples were selected so as to reduce the effect of weathering on the sample. With only a rock hammer, samples further into the face of the rock could not be extracted. Samples were taken from the upper portion of the Lower Pottsville Formation and the upper portion of the Parkwood Formation

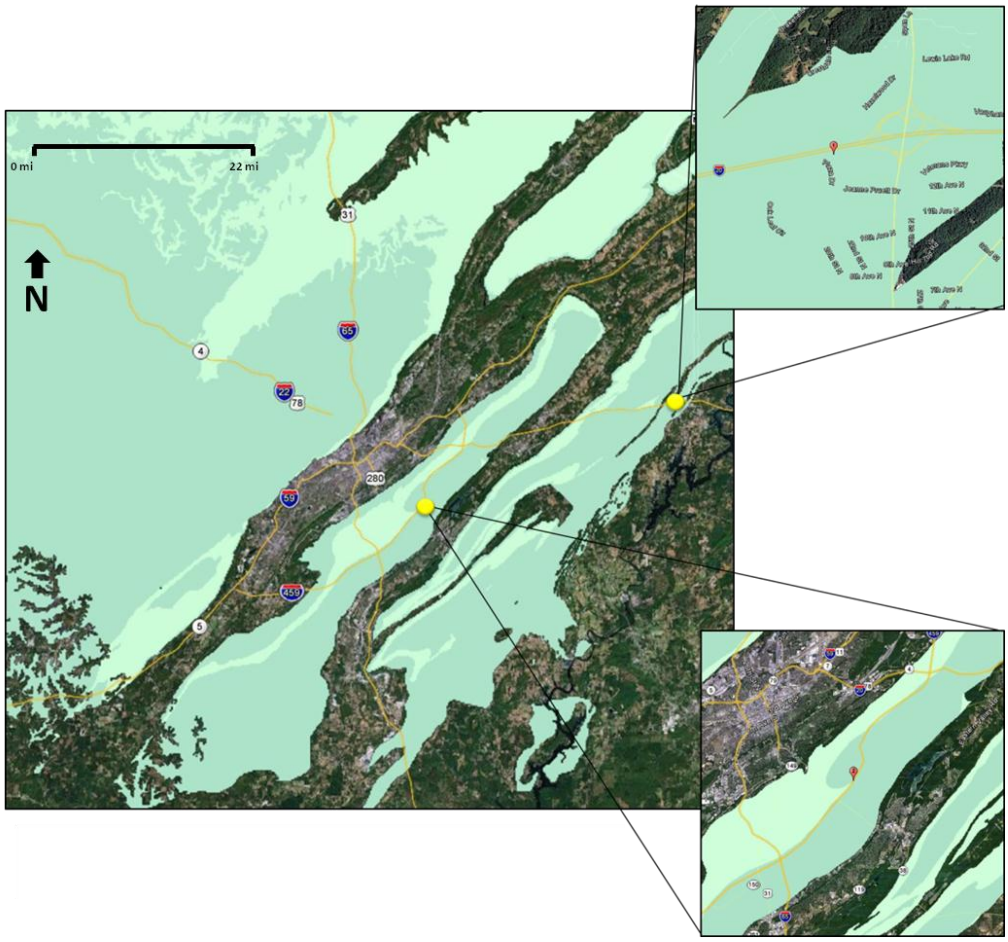

Figure 1-6 Sample Locations

Alabama Geological Survey Map showing sample locations around the Birmingham Area
Parkwood Formation (top) (33˚36'42.44" N, 86˚17' 14.46"W)
Pottsville Formation (bottom) (33˚27'28.92"N, 86˚42'56.78"W)

2 EXPERIMENT

2.1 Procedural Overview

The laboratory experiment (Figure 2-1) focused on two shaley caprocks in the Black Warrior basin. The whole rock was observed as well as the isolated clay fraction. The whole rock was observed using XRD and SEM/EDS. The clay fraction was observed using XRD, XRF, and AA. Changes were monitored in relation to time in order to make inductions regarding the progress of the reaction.

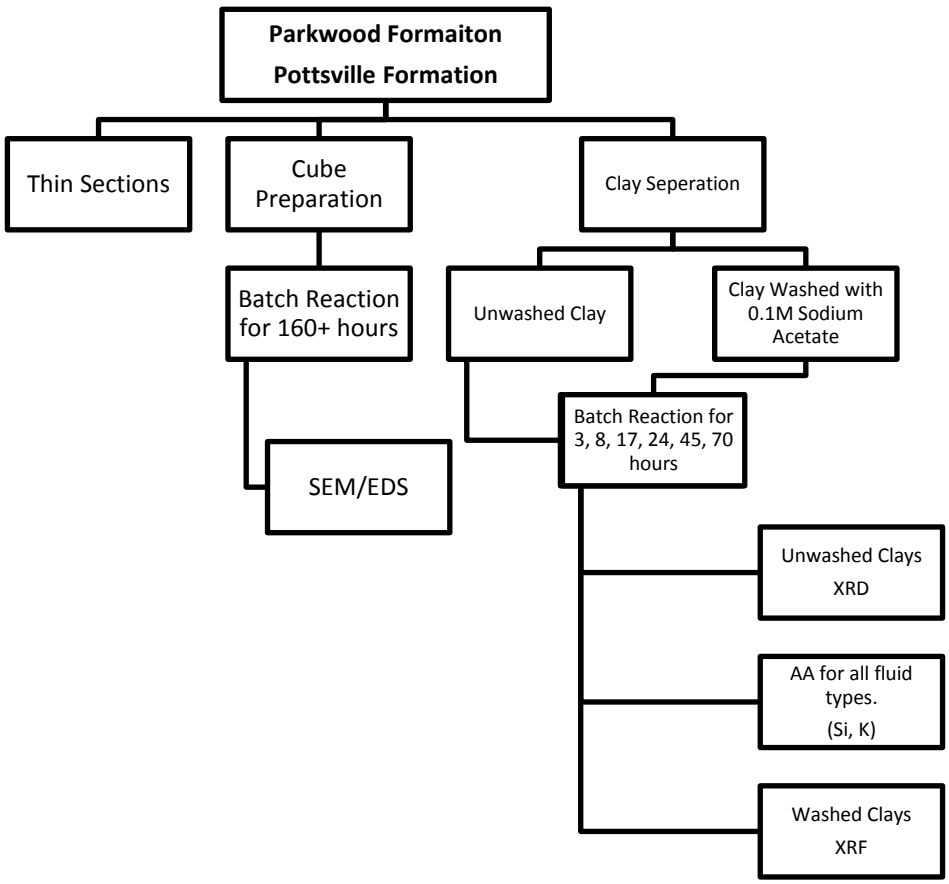

Figure 2-1 Flow diagram of project design.

2.2 Sample Analysis Methods

2.2.1 Thin Section Preparation

Samples of both the Pottsville and Parkwood Formations were prepared by Spectrum Petrographics, Inc.

2.2.2 XRD Analysis

X-ray diffraction (XRD) is the instrumentation typically used for the identification of clay minerals. Diffraction occurs when the wavelength of the X-radiation is roughly the same as the d-spacing of the clay mineral. Bragg's Law gives the angles for coherent and incoherent scattering from the crystal

lattice of a clay mineral. According to Bragg's Law, when there is constructive interference the diffraction and subsequently the d-spacing of the clay mineral can be calculated using the following equation:

$$n\lambda = 2d\ sin\Theta$$

Equation 2-1 Bragg's Law derived.

Where:

$n = order\ of\ reflections\ (Typically, n = 1)$

$\lambda = wavelength\ of\ X - radiation$ Cu Kα = 1.54 Å

$d = d - spacing = \overline{ZB} =$ *the distance between basal layers of the clay*

$2\Theta =$ *the angle of diffraction*

This equation is derived from Figure 2-2:

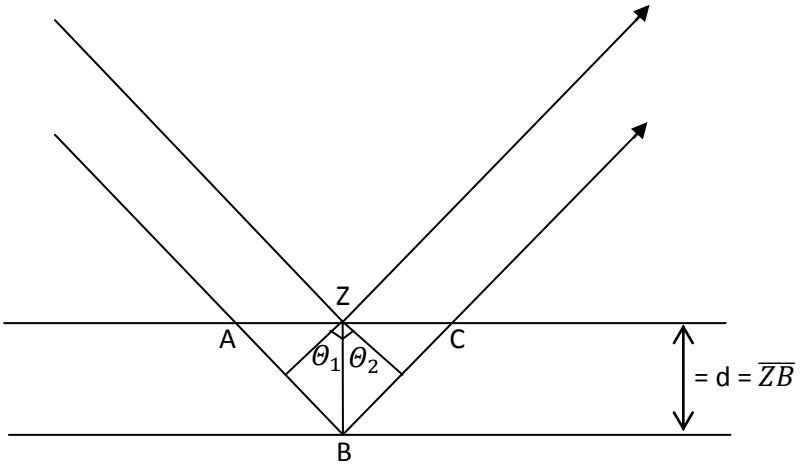

Figure 2-2 X-ray diffraction according to Bragg's Law.

Where:

$Sin\ \Theta_1 = \frac{\overline{AB}}{\overline{ZB}}$

$Sin\ \Theta_2 = \frac{\overline{BC}}{\overline{ZB}}$

$\Theta_1 = \Theta_2$

$n\lambda = \overline{AB} + \overline{BC}$

$\overline{AB} + \overline{BC} = \overline{2\ (\overline{ZB}\ Sin\Theta)}$

To generate X-rays, a cathode with a tungsten filament is heated and electrons are emitted across an X-ray tube at -35kV. The tube is held in a vacuum to permit electron acceleration without ionization. After crossing the tube, the electrons hit a copper anode and are diffracted, emitting characteristic and continuous radiation. Characteristic radiation is emitted when an electron is knocked out of the K-shell and another 'falls' in from the second L-shell (L_2) (Figure 2-3) (Moore and Reynolds, 1997). This drop in the electron causes the emission of an X-ray photon with characteristic CuK_2 radiation. The beam then passes through a beryllium window where radiation such as heat and tertiary X-rays are filtered out. The beam then passes through a monochromater, which limits and directs the beam before it hits the sample (Moore and Reynolds, 1997). The beam then penetrates the sample lattice structure and is scattered by the atoms creating constructive and destructive interference. Constructive interference occurs when two or more rays are in phase and destructive interference occurs when the rays are out of phase (Moore and Reynolds, 1997). When the atoms are not evenly spaced within the lattice, constructive interference cannot occur and therefore no diffraction takes place (Moore and Reynolds, 1997). The beam is adjusted so that only Kα is diffracted off of the sample, then through another monochromater. At this point, the beam enters a databox for analysis.

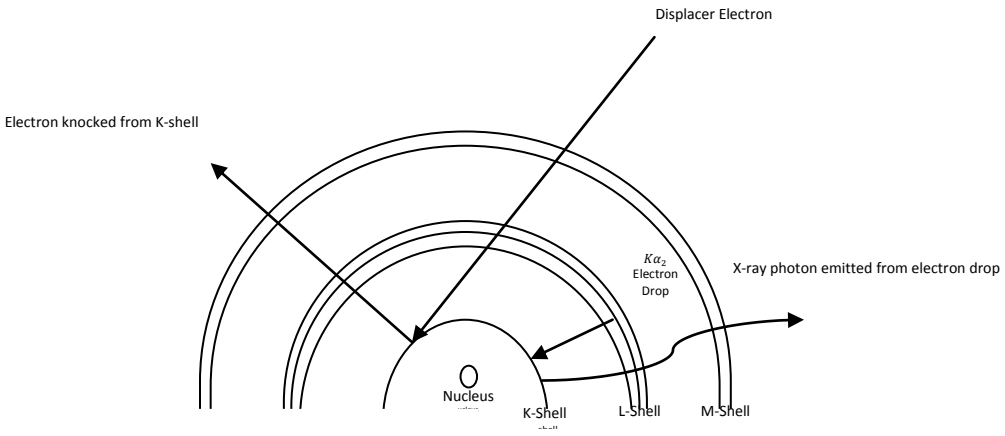

Figure 2-3 Characteristic Radiation
Falling electrons and characteristic radiation (Modified from Moore and Reynolds, 1997)

Two X-Ray diffractometers were used to analyze the samples. The first instrument used was a Philips X-ray Diffractometer with a MDI Databox for computer control and acquisition of diffraction data. The diffractometer was operated at a power rating of 700 Watts and measurements were taken at a step size of 0.02 degrees 2Θ and a step time of 2 seconds from 5-15 degrees 2Θ. The software used for data collection was TALK, and for analysis, JADE. The second instrument used was a PANalytical X'pert Pro. The diffractometer took measurement from 2-32 degrees 2Θ with a 0.007 degree step size and a scan step time of 8.67 seconds. The software used for data collection was the PANalytical software, Data Collector, and for analysis, High Score Plus.

Oriented slides were prepared to promote basal diffraction, or 00*l* reflections. For phyllosilicates, this is the most diagnostic method of slide preparation (Moore and Reynolds, 1997). Random mounts were prepared for whole rock analysis following Moore and Reynolds (1997). The X-ray patterns were interpreted for clay mineralogy information from Moore and Reynolds (1997). Relative abundances of the minerals found in each sample were quantified using the intensities of the illite/smectite (001), illite (001), and kaolinite (002) peaks (Equation 2-2). The values produced from this method are not accurate quantitative estimates, but relative indicators of a change in mineralogy (Spötl *et al.*, 1993).

$$Relative\ abundance\ of\ A = \frac{peak\ area\ A}{peak\ area\ A + peak\ area\ B + peak\ area\ C}$$

Equation 2-2 Relative Abundance Calculation

Peak areas were determined by High Score Plus using a minimum significance of 3, a tip width of 0.2 2Θ, an max tip with of 0.7 2Θ and a peak base width of 1.5 2Θ. These settings accurately isolated

the peaks. Data collected from the Philips X-ray Diffractometer is not included in the body of the analysis, but in Appendix C - Phillips X-Ray Diffractometer Data.

2.2.3 XRF Analysis

Wavelength dispersive (WD) X-ray florescence (XRF), much like XRD, is an analytical technique that introduces a solid sample to an X-ray source (LaTour, 1989, Billets, 2006). The source X-rays have the appropriate energy to cause the sample to emit characteristic X-rays. A qualitative elemental analysis is possible from the wavelength of the characteristic radiation, and a quantitative analysis is possible by analyzing the intensity of a given wavelength (Billets, 2006). K lines are typically used for elements with atomic numbers from 11 to 46, and L lines are used for elements above atomic number47. M-shell emissions are measurable only for metals with an atomic number greater than 57 (Billets, 2006).

WDXRF analyzers have three major components: an X-ray generating source such as an X-ray tube, a detector to convert X-rays emitted from the sample into measurable electronic signals, and a data processing unit to convert fluorescence energy signals into elemental concentrations (Billets, 2006). The X-ray beam interacts directly with the sample. Then, the photoelectrons emitted from the sample are passed through a collimator to direct the beam so as to closely control the collection angle. The beam then hits an analyzing crystal which is angled to disperse incident radiation according to Bragg's Law before being received by the detector (Figure 2-4) (Jenkins, 1985).

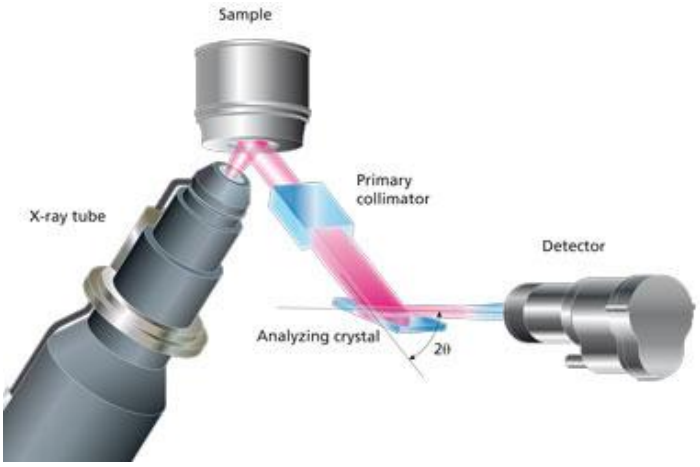

Figure 2-4 WDXRF Spectrometer
(Panalytical, http://www.panalytical.com/index.cfm?pid=313)

The instrument used to perform an XRF analysis was an automated Rigaku 3270 X-ray Spectrometer fitted with a Rhodium X-ray tube. The instrument was operated at 50 kV and 50 mA. Companion software specifically designed for the Rigaku 3270 X-ray Spectrometer was used for analysis. A reference disk was initially tested to minimize any analytical error, namely the interference of distinct elements causing the absorption or enhancement of fluorescent radiation or spectral overlap. This reference disk, or 'alpha correction,' was used to ensure a linear calibration curve (LaTour, 1989). The Rigaku 3270 system automatically performed calculations to correct for overlap and mass absorption effects, and peak intensities measured by the spectrometer were converted to oxide concentrations by the companion software (LaTour, 1989).

2.2.3.1 XRF Data Treatment

Structural formula data was calculated using a procedulre for a 2:1 layer silicate with having a formula unit with 11 oxygens, 8 from the tetrahedral and 3 from the octahedra. The structural formula developed is not a true mineral structure but an average. This is because the clay mixture is not homogenous and contains impurities. The formula from Moore and Reynolds (1997) is as follows:

$$\frac{Formula\ Weight}{Cation\ Valence\ Charge} = \boldsymbol{Equivalent\ Weight}$$

$$\frac{Weight\ \%\ Oxide}{Equivalent\ Weight} = \boldsymbol{Atomic\ Proportion\ Cation\ Charge}\ (\boldsymbol{APCC})$$

$$\frac{\int_x^y APCC}{22} = \boldsymbol{Normalization\ Factor}$$

$$\frac{Equivalent\ Weight}{Normalization\ Factor} = \boldsymbol{Cation\ Charge\ Formula\ Unit}\ (\boldsymbol{CCFU})$$

$$CCFU * Oxygen\ Number = \#\ \boldsymbol{Cations\ in\ Formula\ Unit}$$

Equation 2-3 Calculation of structural formula
From Moore and Reynolds (1997)

2.2.4 AA Analysis

Atomic absorption spectroscopy uses the principles of atomic absorption of light to determine how much of a metallic analyte is present in a sample. Liquid samples are extracted and atomized in a graphite furnace. The vaporized samples then interact with a light of a specific wavelength for the metal to be observed. By exciting the outermost electron orbits of the metals and pushing the orbits into a higher energy level (congruent with the wavelength of the light), some of the metals' electrons absorb a portion of the light. This causes less light to leave the flame than was originally present, and this difference is indicative of the amount of the analyte in the original solution. The absorption of light is directly proportional to the amount of analyte in the solution. Concentration measurements are determined by creating a concentration curve with standards of a known concentration. The concept of the proportionality of the adsorption coefficient of a solution to its concentration was demonstrated by August Beer in 1952 through Beer's Law (Maikala, 2010). For this experiment, Si, and K were the ions to be analyzed. The wavelengths for Si, and K are 251.6 nm and 766.5 nm, respectively. A Perkin Elmer Atomic

Absorption Spectrometer 3110 was used to analyze all sample solutions. The Perkin Elmer Atomic Absorption Laboratory Benchtop (1985) software program processed the data.

2.2.5 SEM/EDS Analysis

A scanning electron microscope (SEM) functions by bombarding the sample with primary electrons in a scanning pattern (Figure 2-6). A beam of electrons is produced at the top of the microscope by an electron gun. The electron beam follows a vertical path through the microscope, which is held within a vacuum. The striking electron causes the emission of secondary electrons. The height and slope of the object determine the number of secondary electrons generated per unit time, and the velocity of those electrons. The beam hitting the sample causes electrons and X-rays to be ejected from the sample. Detectors collect the X-rays, backscattered electrons, and secondary electrons and convert them into a signal that is translated to an image produced on a screen similar to that of a television (Iowa State University, 2009). This is the final image produced for analysis.

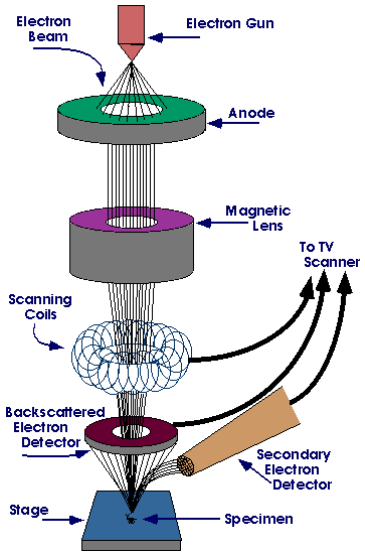

Figure 2-5 Anatomy of a SEM
From: http://www.purdue.edu/rem/rs/sem.htm#2

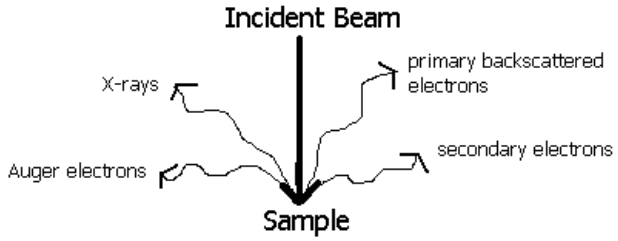

Figure 2-6 Example of characteristic scattering
From: http://www.purdue.edu/rem/rs/sem.htm#2

All samples were sputter coated with a carbon film, analyzed using a LEO 1450 VP Scanning Electron Microscope (SEM)and were also analyzed using Energy-dispersive X-ray spectroscopy (EDS). Fragments of the whole rock were used for SEM/EDS analysis. SEM accelerating voltage was set at 20.0 kV. Probe current for EDS was 5 nA with a beam current 80 mA. Software used to analyze the SEM was Zeiss Smart SEM, EDS analytical software was IXRF 'Iridium'.

2.3 Sample Preparation

2.3.1 Clay Preparation

Whole rock samples were crushed and then powdered in a shatterbox. Samples were disaggregated with a Branson Sonifier. Roughly 15 mL of sample were added to 200 mL of $_{di}H_2O$ and sonified at 71% amplitude for five minutes. The sample was then centrifuged at 1000 rpm for 5 minutes to remove the sample fraction >1µm. The supernatant was then centrifuged again at 8500 rpm for 20 minutes to separate the fluid from the remaining fine grained sample. This method roughly follows Moore and Reynolds, 1997 and Deocampo *et al.* 2010.

2.3.1.1 Sodium Acetate Wash

A 0.1M sodium acetate (CH_3COONa) wash was used to remove ions adsorbed in an exchangeable state to the clays. Separated clay from each formation (about 4 grams) was added to 500 mL of the

sodium acetate solution and stirred for 0.5 hours. Samples were then filtered through a 0.4 µm Millipore filter and then added to 200 mL of $_{di}H_2O$. To reverse the effects of flocculation, samples were sonicated in the $_{di}H_2O$ at 70% amplitude for two minutes. Samples were filtered with a 0.4 µm filter for a second time before they were dried at 90° C for 24 hours, ground with a mortar and pestle and stored in a desiccator. This was done to allow for a comparison of the brine of the untreated clay with the brine of the treated clay, post- experiment.

2.3.2 Cube Preparation

Random samples of both the Pottsville and the Parkwood Formations were cut into one centimeter cubes for experimentation. The cubes were then treated in the batch reactor with just brine or brine and supercritical CO_2. Reaction times were between 159-167 hours. This method came from Massarotto *et al.* (2010), but the remainder of the laboratory procedure was not followed. Massarotto *et al.* (2010) observed the changes in permeability and crystalinity in coal that came with exposure to $_{di}H_2O$ and CO_2.

2.3.3 Batch Reactions

A Parr Instruments High Strength Acid Digestion Vessel was used to run the experiment in a Lindberg/Blue electric oven. The digestion vessel contained a 23 mL Teflon cup. Teflon cups were pre-treated with CO_2 so as to test the amount of absorption into the porous cup (Giammar *et al.*, 2005). The pre-treated cup was weighed before the application of CO_2 and after. No significant change in weight occurred (Table 2-1), so the treatment was not used again.

Table 2-1 Treatment of Teflon Cups with CO_2

Pre-Treatment Weight	Mass CO_2	Post-Treatment
100.16 g	1.89 g	100.8 g

Suspended concentrations of clay were held between 20g/L and 30g/L (following Gimmar *et al*, 2005), meaning that 0.4-0.5g of sample were added. Variation in sample mass was considered insignificant. Given that the average density of silicates is about 2.65 g/cm^3, the mass of sample added would result in a change of volume between 0.15-0.20 mL using the following formula:

$$volume = \frac{mass\ sample}{density\ sample}$$

Equation 2-4 Formula to calculate the total volume of clay.

This change in volume was considered to be small enough that small changes in the mass of the sample would not have significantly altered the pressure inside of the vessel.

Weighed portions of CO_2 were used to produce 120+ bar pressure within the Teflon cup at 90°C. Pressure calculations are shown in Appendix B - Batch Reaction Pressure Calculations. The volume of the container was 23 mL and 5 mL was left for headspace CO_2. In order to maintain the standard concentrations, 0.5 g of solids was added to 18 mL of brine. The brine was first frozen in the cup so as to prevent the rapid sublimation of the dry ice.

pCO_2 was controlled by the headspace of CO_2, using initial ambient atmosphere and the change in pressure which was a product of the phase change of solid CO_2 to gas. Pressure in the reactor was calculated from the known volume of the reactor, brine, and the measured mass of CO_2 at 363 K and 100 bar using the Ideal Gas Law (Equation 2-44). The solubility of CO_2 at 363 K and 100 bar was determined by Duan and Sun (2003) to be 0.8219 mol CO_2/kg H_2O. Pressure was maintained at roughly 120 bar for the clay experiments and 140 bar for the experiments using a 1 cm^3 cube of sample. Some CO_2 loss occurred during the transfer from scale to pressure cup, so there was no way to exactly measure the amount of CO_2 entering the vessel, but the loss is assumed to be negligible.

$$Pv = nRT$$

Equation 2-5 Ideal Gas Equation

Where:

$P = absolute\ pressure\ of\ the\ gas$

$v = volume$

$n = number\ of\ moles\ of\ gas$

$R = ideal\ gas\ constant$

$T = temperature$

Clay samples were subjected to the simulated sequestration conditions over 3, 8, 17, 24, 45, and 70 hour time periods, and whole rock cubed samples were subjected for 165+ hours (Appendix F). The time required for the temperature of the digestion vessel to reach 363K was not taken into account. Parr Instruments High Strength Acid Digestion Vessel is a closed system which prevented the measurement of the temperature inside of the Teflon cup during experimentation; therefore, the exact time of temperature equilibration was not known. After the experimental run time, the vessel was allowed to cool for an hour in order to reduce the pressure and temperature of the instrument so that it could be opened. The samples were then filtered and prepared accordingly.

2.3.4 Brine Composition

The experimental brine was modeled after brine data published by Pashin (1991b). For the model brine, Cedar Cove Field at 3,115 feet depth was used (Table 2-2). Brine solution was prepared with ultrapure (18 MΩ cm) water. The brine mixture was heated to a slow boil in a 1000 mL beaker with a watch glass covering it to force the salts into solution. Some of the salts would precipitate, so the brine was stirred on a stir plate with a stir bar before removing a portion for an experiment.

Table 2-2 Brine Composition

Chemical	Concentration (g/L)
NaCl	11.69
Na2CO3	0.53
CaCl2 1M solution	1.11
MgCl2 1M solution	0.48

2.3.5 XRD Sample Preparation

Samples not rinsed by sodium acetate were used for the XRD experiments. After the reaction, samples were wet mounted on slides and analyzed using XRD.

2.3.6 XRF Sample Preparation

The sample preparation roughly followed the methodology outlined by La Tour (1989). Prior to XRF disc preparation, a loss on ignition was performed at 1100˚C for 60 minutes. This was done to remove any excess organic matter or water from the clay structure. Fused discs were prepared for analysis because fused discs allow a homogenous distribution of elements. This ensures a more accurate analysis of the sample. To make the fused disk, 0.5 g of sample was added to 4.5 g of lithium tetraborate. This mixture was heated in a 95% Platinum (Pt), 5% Gold (Au) crucible at 1000˚C for 15 minutes in a high temperature furnace, including a stirring period at 10 minutes. This homogenous mixture was then poured into a preheated mold to form the sample disc. Once the disc was formed, it was stored in a desiccator.

2.3.7 AA Sample Preparation

The brines of all reactions were separated from the experimental slurry by using a Nanopure filtration system. Samples treated with sodium acetate were filtered with a 0.2 µm filter, and samples left untreated were filtered with a 0.4 µm filter. Different filters were used because it was discovered that during the $_{di}H_2O$ rinse, clay from samples treated with sodium acetate passed through the 0.4 µm filter.

Thus a finer filter was required (0.2 μm) for filtrations handling the sodium acetate washed clay. During the AA testing of the brines, it was noticed that ions, specifically K, were sticking to the sides of the test tubes, and skewing the results. Therefore, one drop of laboratory grade nitric acid was added to each sample tube to prevent cation adsorption to the surface of the bottles.

2.3.8 SEM/EDS Sample Preparation

Cubes of both the Pottsville and Parkwood post-experimental procedure were broken into small fragments for analysis. Samples were treated with a thin carbon film prior to analysis and mounted so that the interior portion of the cube would be analyzed.

3 RESULTS

3.1 Thin Section

3.1.1 Pottsville Formation

In thin section, large quartz crystals are observed in a very fine grained matrix (Figure 3-1). Sedimentary structures including cross-bedding, ball and pillow structures and flame structures are present (Figure 3-2).

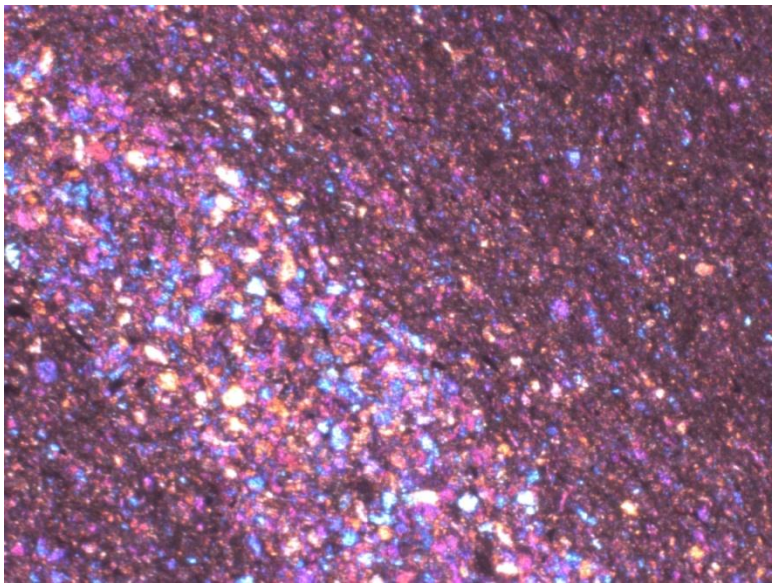

Figure 3-1 Pottsville Formation in Cross Polarized Light (100x)

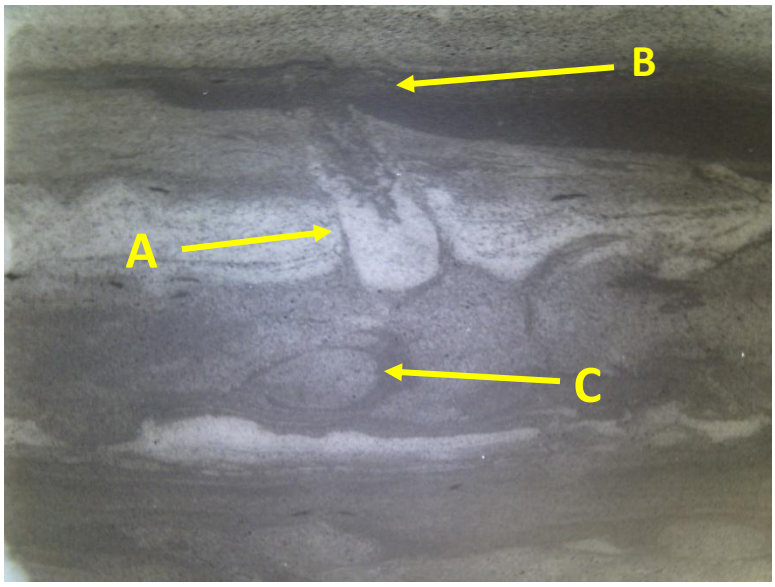

Figure 3-2 Pottsville Formation Sedimentary Structures (actual size)
A.) Flame Structure (B.) Ball and Pillow Structure (C.) Cross-bedding

3.1.2 Parkwood Formation

In thin section, the Parkwood Formation shows very large quartz crystals caught in a fine-grained matrix (Figure 3-3). The sedimentary structures of the Parkwood formation are more simple than the Pottsville Formation, with only cross-bedding present (Figure 3-4).

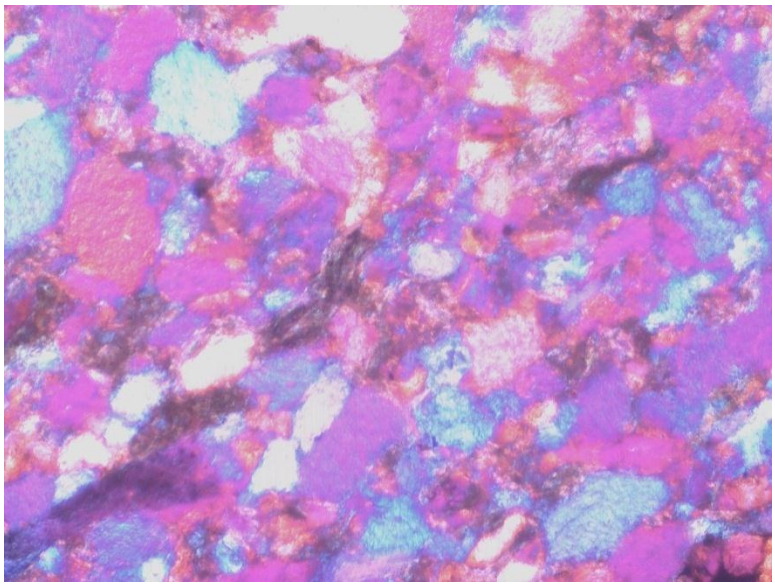

Figure 3-3 Parkwood Formation in Cross-polarized Light (100x)

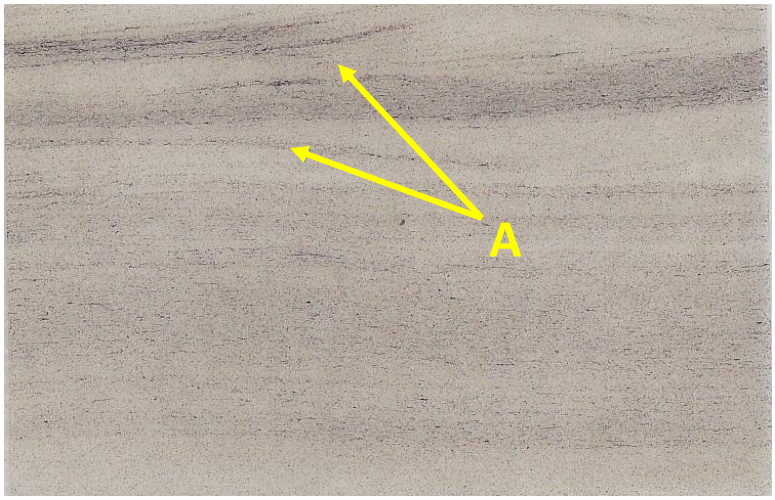

Figure 3-4 Parkwood Formation Sedimentary Structures (2x)

A.) Cross-bedding

3.2 Whole Rock Mineralogy

Random mounts of both the Pottsville and the Parkwood formations were graphed using High Score, and clay mineral estimations were made using the software as well. The Pottsville Formation was shown to have a mixture of muscovite, vermiculite, and quartz. The Parkwood Formation was shown to have the same composition. Individual peaks are labeled and identified in Appendix D - PANalytical X-Ray Diffraction . These identifications however are incorrect. The identification of muscovite is actually the recognition of a 10 Å clay, illite. The identification of vermiculite is actually the recognition of the 14 Å phase of a clay, chlorite.

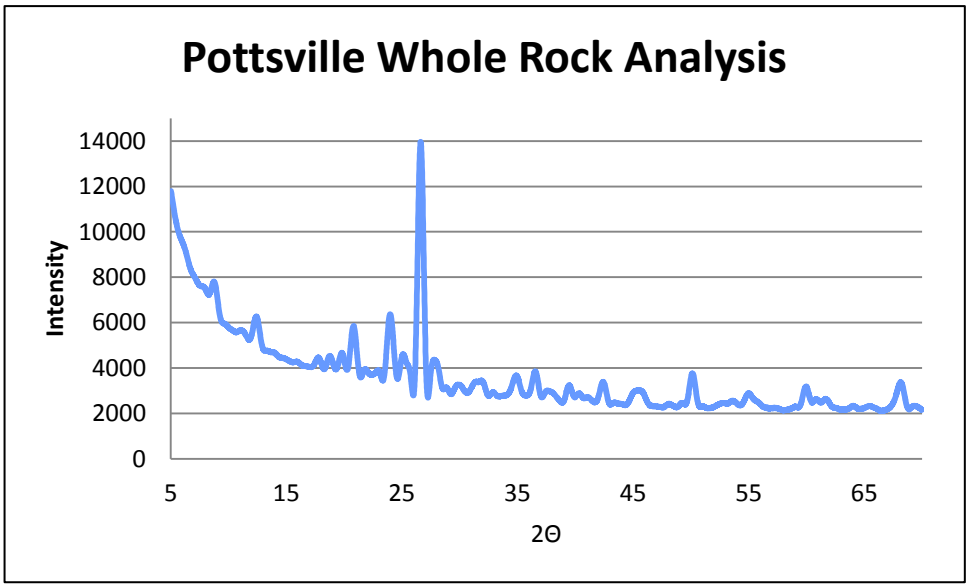

Figure 3-5 Pottsville Whole Rock XRD Pattern

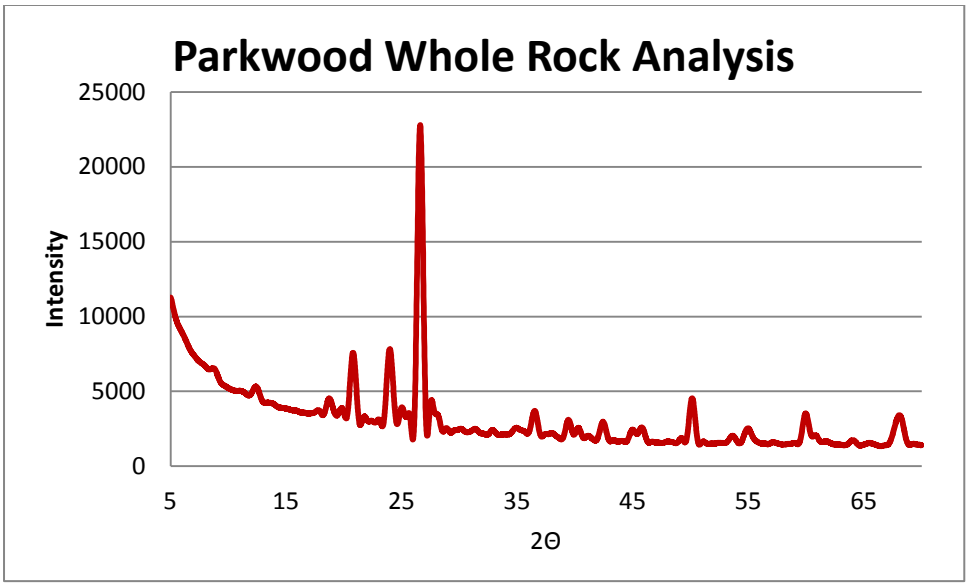

Figure 3-6 Parkwood Whole Rock XRD Pattern

3.3 Fluid Chemistry

Ions of potassium (K) and silica (Si), previously absent in the starting brine solution, appeared in all solutions at 3, 8, 17, 24, 45, and 70 hours, indicating the dissolution of reacting solids (raw data available in Appendix G - Atomic Absorbance Data). Rapid dissolution of both silica and potassium were evident in each sample. The amount of each cation entering solution is given in Table 3-1.

Silica, in all cases, quickly entered into the brine, and in less than 20 hours, its dissolution slowed (Figure 3-7). Samples washed with sodium acetate exhibited a slightly higher rate of dissolution, but were proportionally similar to the untreated samples, indicating the same reactions.

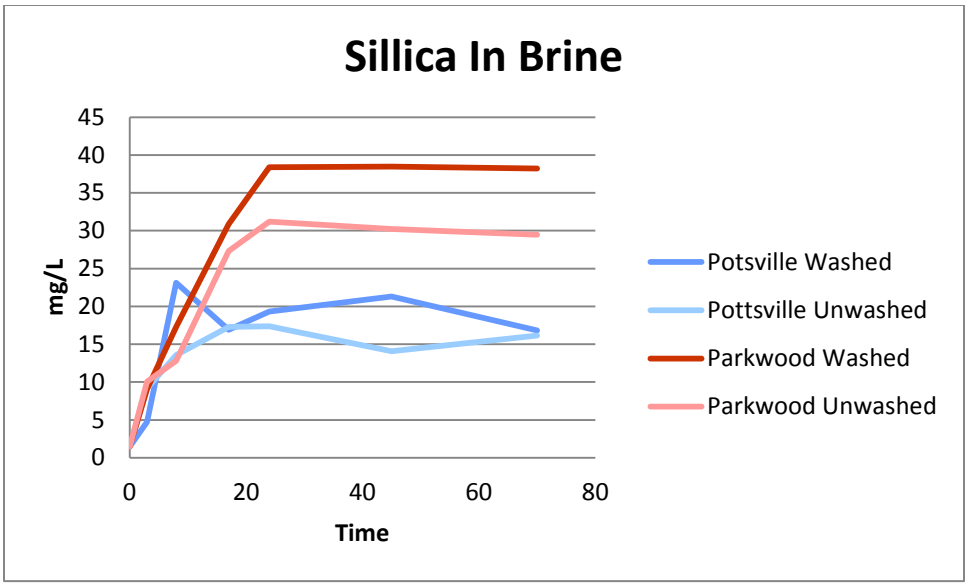

Figure 3-7 AA Detection of Silica in Brine

Potassium, in all cases, rapidly entered the brine (Figure 3-8). After the first three hours, the amount of potassium showed significantly lower rates of change. The clays washed with sodium acetate exhibited a lower rate of dissolution.

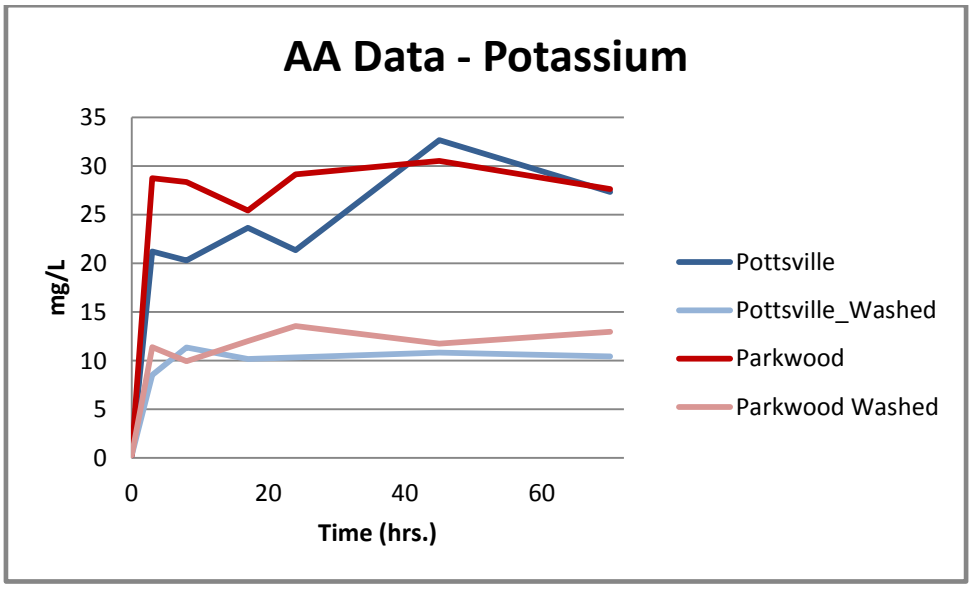

Figure 3-8 AA Detection of Potassium in Brine

Si and K data suggest that the brine reaches a near equilibrium state around 24 hours after the experimental start time. A comparison of the molar ratio of K:Si in idealized illite (~0.2) to the same ratio in the stabilized brine average (

Table 3-1) shows that though illite might be the contributor of K to the brine system, the amount of Si is low and suggests a reprecipitation of a siliceous mineral.

Table 3-1 Si, K Composition of Brine

	Exposure Time	ppm Si	mmol/L Si	ppm K	mmol/L K	Stabilized Average K/Si
Pottsville Unwashed	**0**	1.46	0.05	0.29	0.01	**1.23**
	3	9.19	0.33	21.21	0.54	
	8	13.58	0.48	20.29	0.52	
	17	17.27	0.61	23.66	0.61	
	24	17.36	0.62	21.34	0.55	
	45	14.09	0.50	32.65	0.83	
	70	16.15	0.58	27.34	0.70	
Pottsville Washed	**0**	1.46	0.05	0.29	0.01	**0.39**
	3	4.73	0.17	8.54	0.22	
	8	23.11	0.82	11.36	0.29	
	17	16.93	0.60	10.19	0.26	
	24	19.33	0.69	10.34	0.26	
	45	21.31	0.76	10.81	0.28	
	70	16.84	0.60	10.45	0.27	
Parkwood Unwashed	**0**	1.46	0.05	0.29	0.01	**0.69**
	3	10.05	0.36	28.73	0.73	
	8	12.80	0.46	28.34	0.72	
	17	27.32	0.97	25.41	0.65	
	24	31.19	1.11	29.15	0.75	
	45	30.24	1.08	30.50	0.78	
	70	29.47	1.05	27.63	0.71	
Parkwood Washed	**0**	1.46	0.05	0.29	0.01	**0.24**
	3	9.11	0.32	11.39	0.29	
	8	17.27	0.61	9.95	0.25	
	17	30.85	1.10	12.01	0.31	
	24	38.41	1.37	13.55	0.35	
	45	38.49	1.37	11.75	0.30	
	70	38.23	1.36	12.98	0.33	

3.4 Solid Phase Reactions

3.4.1 XRD Clay Analysis

Peak data is available in Data 'Clay Mineral Peak Data.' Both samples show similar clay compositions (Figure 3-9 and Figure 3-10). X-ray diffraction analysis of ethylene Glycol solvated samples failed to identify smectite in these clays. Two peaks around 6.1 2Θ, 14.3 Å and 8.7 2Θ, 10.1 Å represent chlorite

(001) and illite (001) respectively. The peak around 12.4 2Θ could represent kaolinite (001) or chlorite (002) or a mixture of both. However, the large peak around 12.4 2Θ, 7.1 Å likely represents Fe-chlorite (Chamosite) since Fe-chlorite, as opposed to Mg-chlorite, has even peaks which dominate in intensity over the odd peaks (Moore and Reynolds, 1997). The peak located at 18.8 2Θ 4.74 Å also suggests the presence of chlorite over kaolinite (Moore and Reynolds, 1997). Illite presence is confirmed by its (001) and (002) peaks at 8.8 2Θ, 10.1Å and 17.7 2Θ, 5.0 Å. The quartz (022) peak was barely present above the 'noise' of the graph, but was accounted for, showing only a faint peak on average around 19.5 2Θ, 4.2 Å (Moore and Reynolds, 1997).

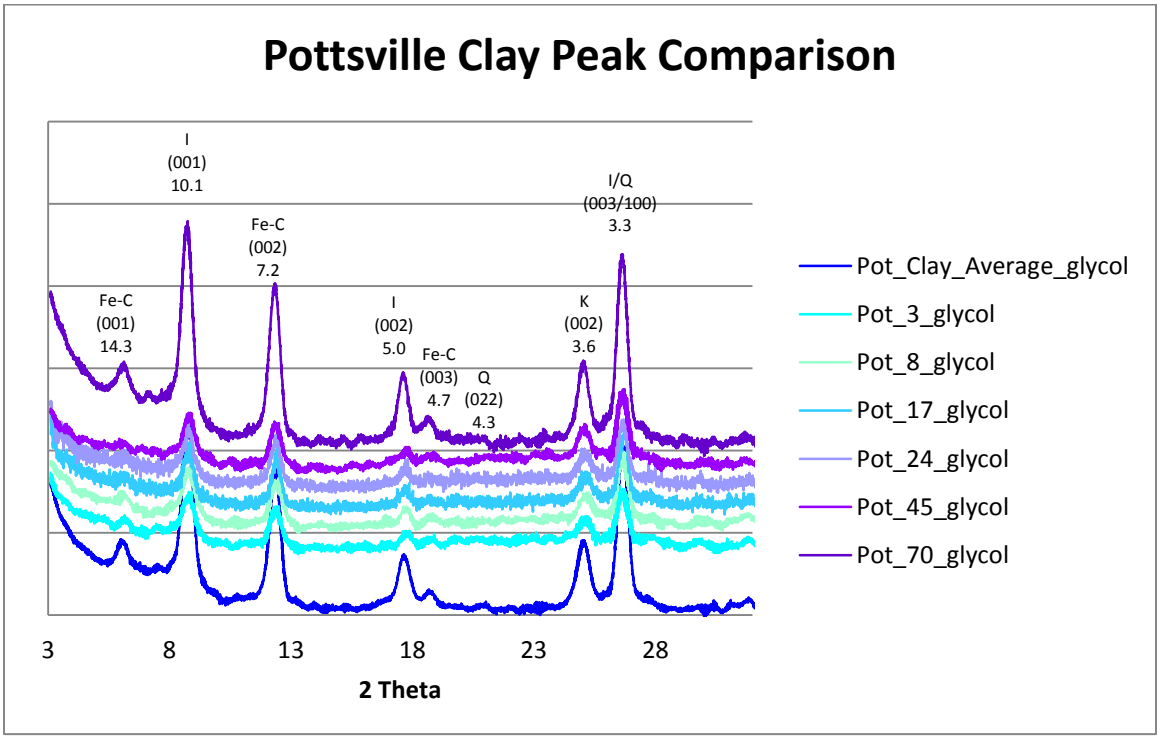

Figure 3-9 Pottsville Clay Peak Comparison with average d-spacing Angstroms

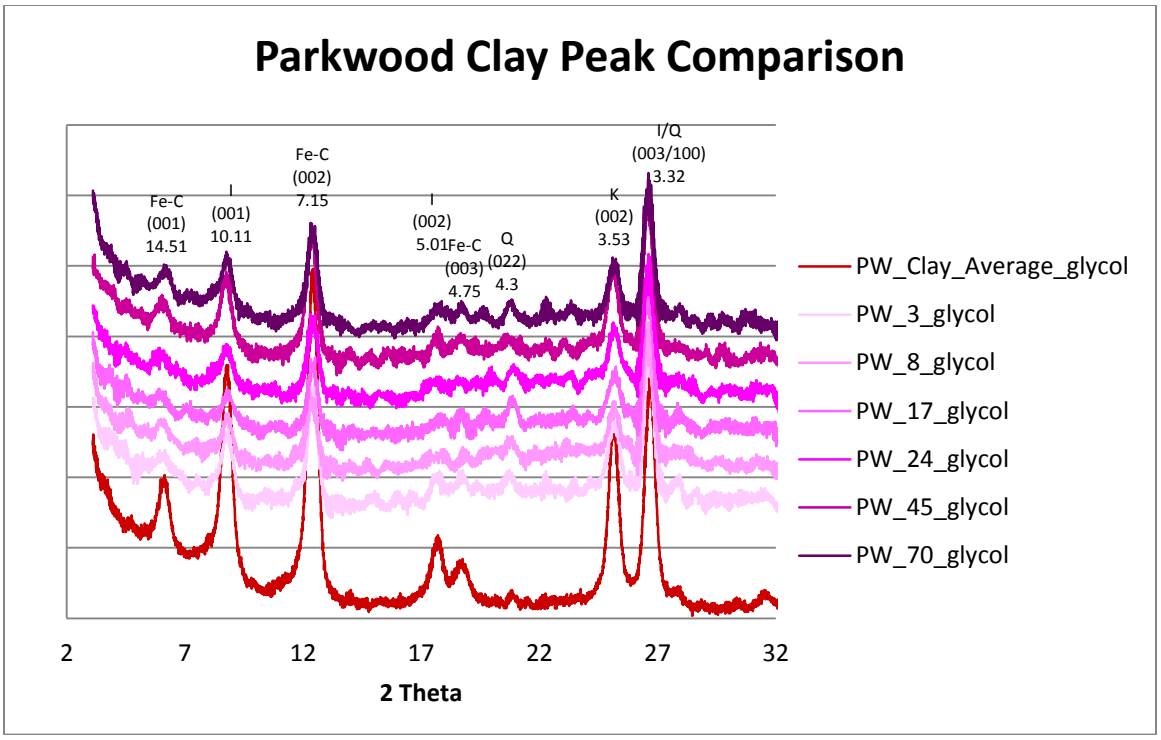

Figure 3-10 Parkwood Clay XRD Peak Comparison with Average d-spacing in Angstroms

3.4.1.1 Relative Abundance of Clay Minerals

Relative to the illite (001) peak and the kaolinite (002) peak, Fe-chlorite (002) abundance increased in both samples for the first 17 hours before it began to reduce (Figure 3-11). Illite decreased, relatively, before increasing in both samples over the last experimental run time from 45 to 70 hours (Figure 3-12). Kaolinite increased in relative abundance before decreasing during the last experimental run time (Figure 3-13). Although some variations are observed, no wholesale clays are noted, and the basic clay assemblage remains.

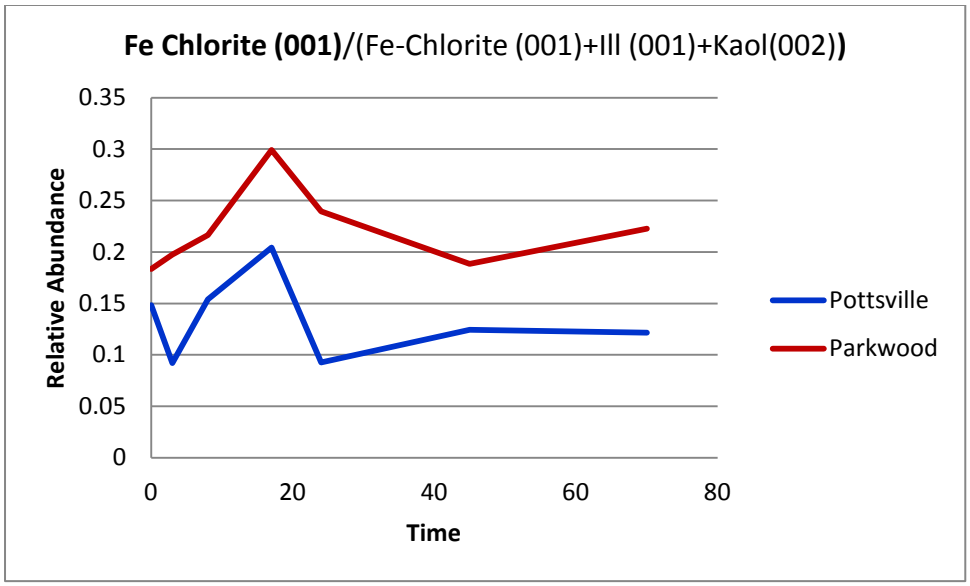

Figure 3-11 Relative Abundance – Fe-Chlorite (001)

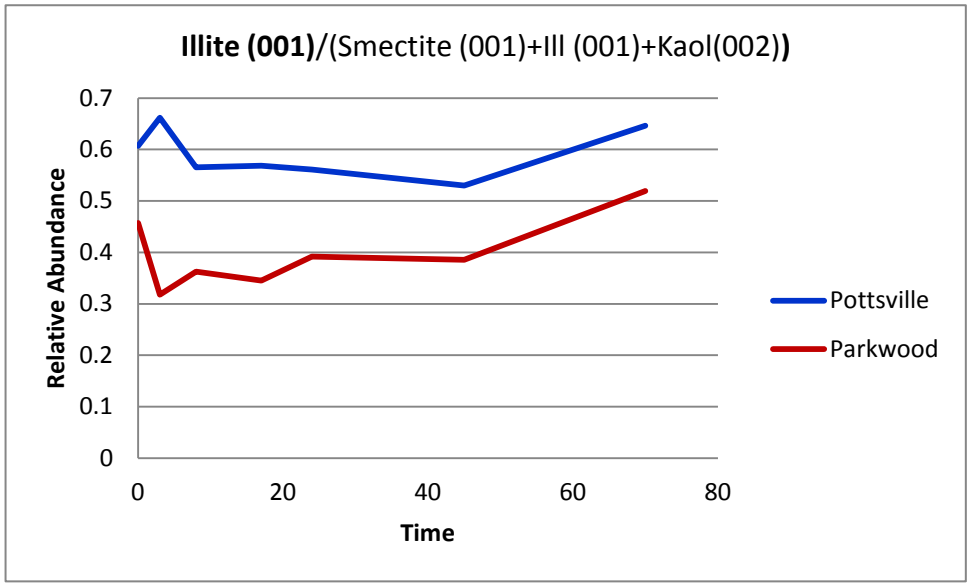

Figure 3-12 Relative Abundance - Illite (001)

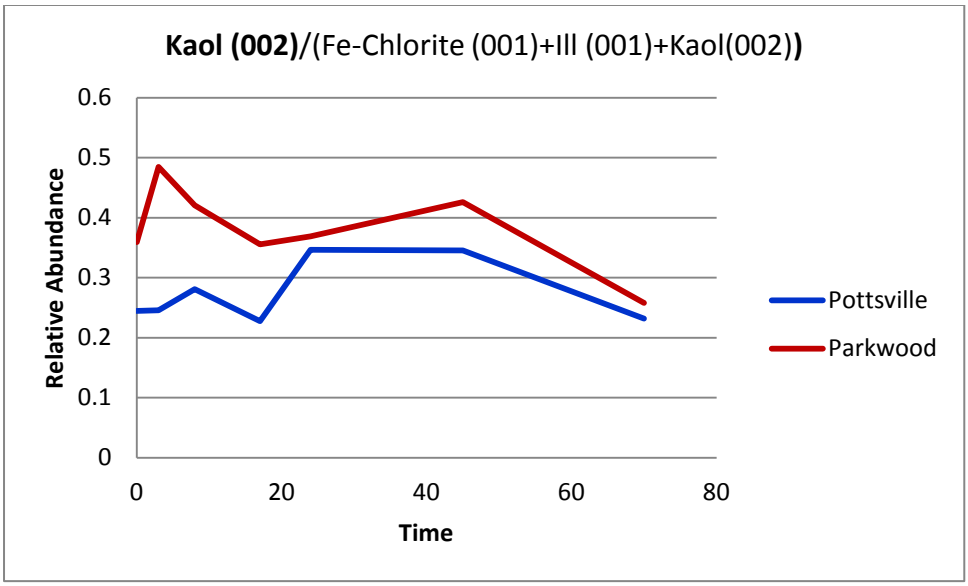

Figure 3-13 Relative Abundance - Kaolinite (002)

3.4.2 XRF data

Octahedral compositions of the clay minerals are shown through the calculation of structural formulas of layer silicates assuming a 2:1 structure formula unit of 11 oxygen atoms (Moore and Reynolds, 1997, Deocampo, 2004) (Table 3-2). The Pottsville and the Parkwood formations plot closely on a triplot of their octahedral components (Al, Fe, Mg) (Figure 3-14), but magnesium has very little effect on the octahedral composition of the clay, lending the octahedral sheet to be classified as *gibbsite-like*. The Octahedral Cation Index (OCI), an expression of the octahedral composition of any clay (Deocapmo, 2004), was plotted against time to demonstrate the lack of change with respect to time (Figure 3-15). One outlier was excluded (Pottsville 3 hr.). Figure 3-16 shows the relation of only Fe and Al with the outlier, Pottsville 3 hr, excluded. The Pottsville Formation shows a higher ratio of Fe to Al, but there is no significant change in the relation of octahedral composition of these clays to time (Figure 3-17) when excluding Mg from the analysis.

Table 3-2 Clay Mineral Structural Compositions

Showing the number of cations per formula unit based on an average structure.

	Tetrahedral			Octahedral			Interlayer Cation			OCI
	Si	Al	Al	Ti	Fe	Mg	Ca	Na	K	
Pottsville										
0	3.27	0.73	1.46	0.05	0.51	0.25	0.02	0.07	0.50	0.13
3	3.31	0.69	4.07	3.35	2.53	2.47	3.89	0.72	1.69	0.37
8	3.23	0.77	1.40	0.06	0.54	0.25	0.04	0.14	0.53	0.13
17	3.28	0.72	1.41	0.05	0.52	0.24	0.08	0.13	0.48	0.13
24	3.27	0.73	1.41	0.05	0.53	0.24	0.08	0.13	0.49	0.13
45	3.27	0.73	1.42	0.05	0.52	0.24	0.07	0.14	0.48	0.12
72	3.27	0.73	1.41	0.05	0.52	0.24	0.09	0.13	0.48	0.12
Parkwood		.								
0	3.96	0.04	1.42	0.05	0.40	0.18	0.01	0.10	0.29	0.10
3	3.83	0.17	1.39	0.05	0.44	0.20	0.05	0.14	0.31	0.11
8	4.13	0.00	1.27	0.04	0.35	0.16	0.04	0.15	0.25	0.10
17	3.81	0.19	1.37	0.05	0.45	0.20	0.05	0.16	0.32	0.11
24	3.83	0.17	1.41	0.05	0.44	0.19	0.03	0.14	0.31	0.10
45	4.04	0.00	1.36	0.05	0.37	0.17	0.05	0.15	0.26	0.10
72	3.80	0.20	1.37	0.05	0.45	0.21	0.06	0.14	0.32	0.12

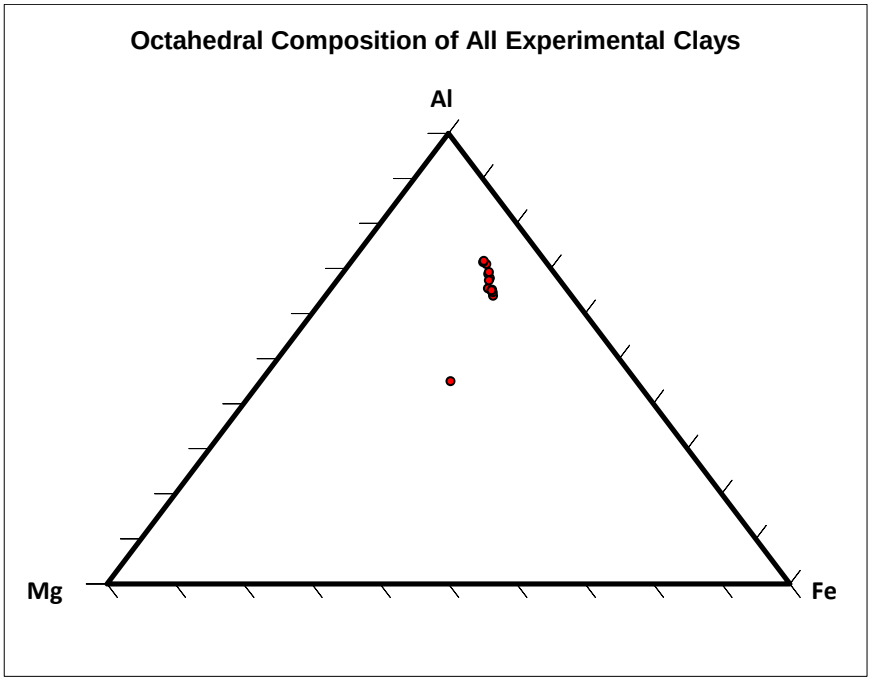

Figure 3-14 Tri-Plot of All Experimental Clay Composition

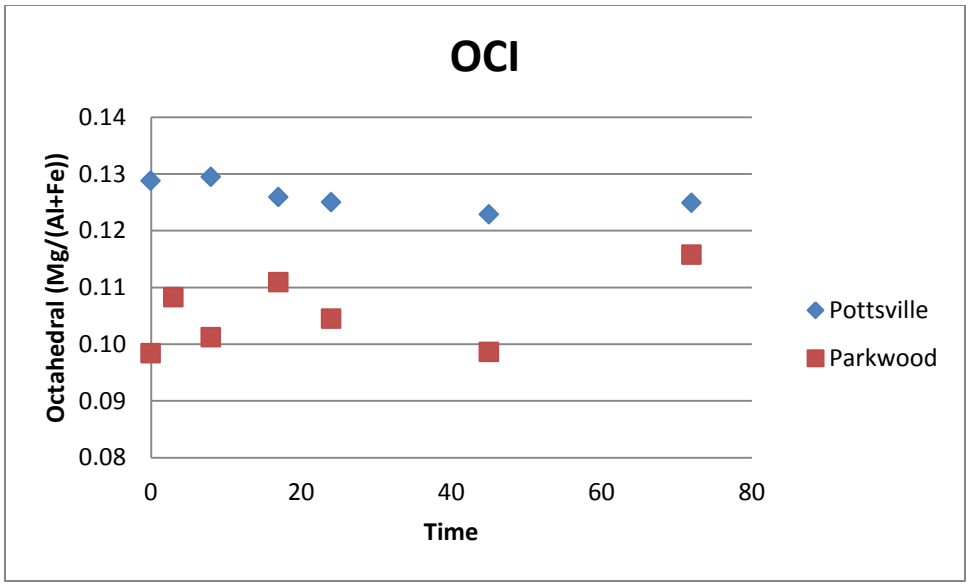

Figure 3-15 Octahedral cation index of clay in relation to time.

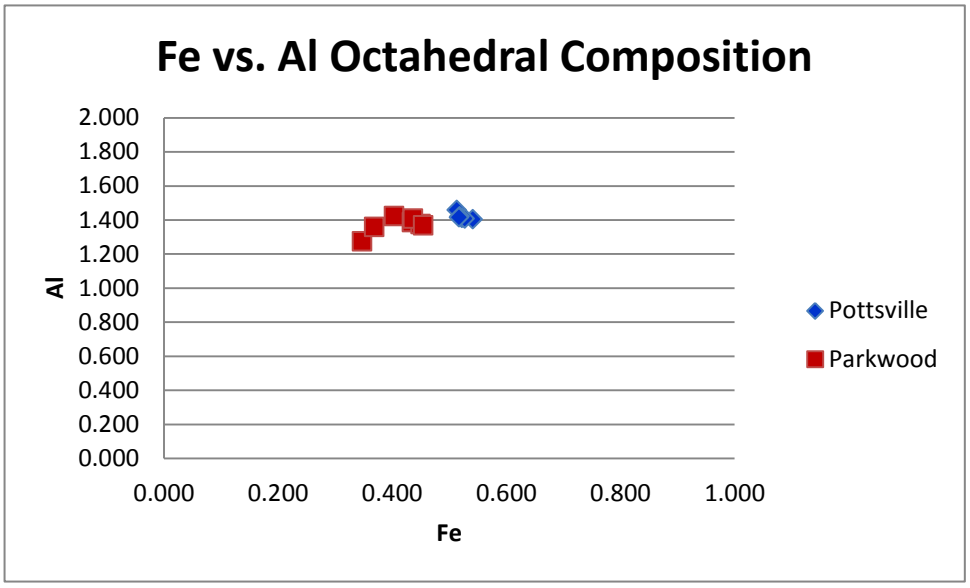

Figure 3-16 Octahedral Composition Fe/Al

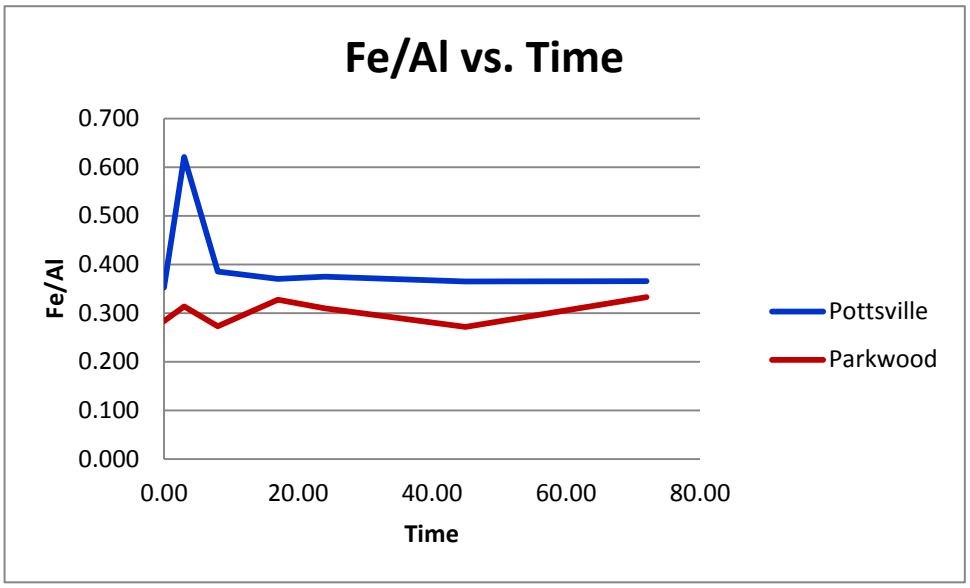

Figure 3-17 Fe2O3/Al2O3 vs. Time

Tetrahedral composition of the clays are compared by plotting the number of cations per formula unit of Si and Al (Figure 3-18). The individual clays cluster with a higher ratio of Si to Al in the Pottsville Formation. There is a greater amount of change in the tetrahedral sheet cations than in the octahedral, but nothing significant (Figure 3-19).

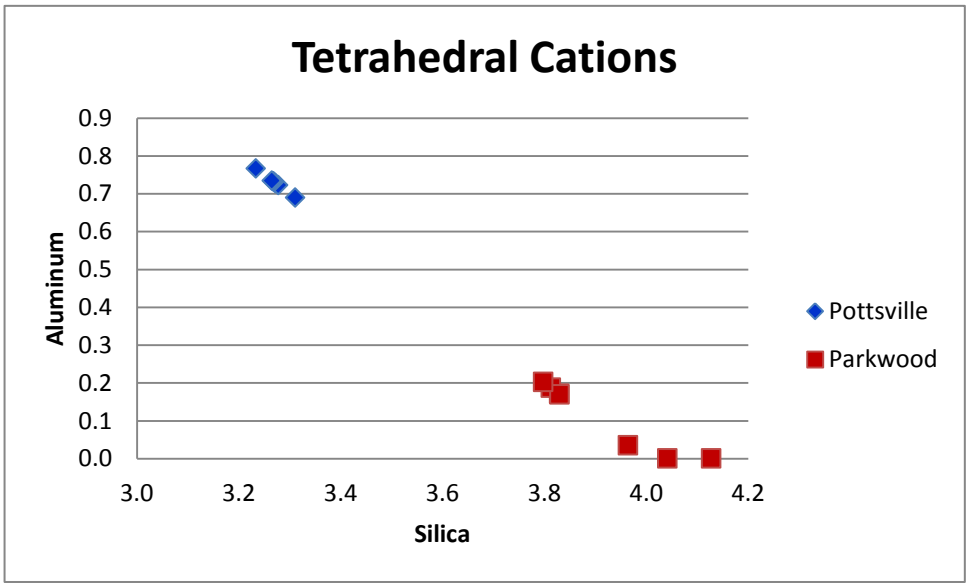

Figure 3-18 Tetrahedral Composition

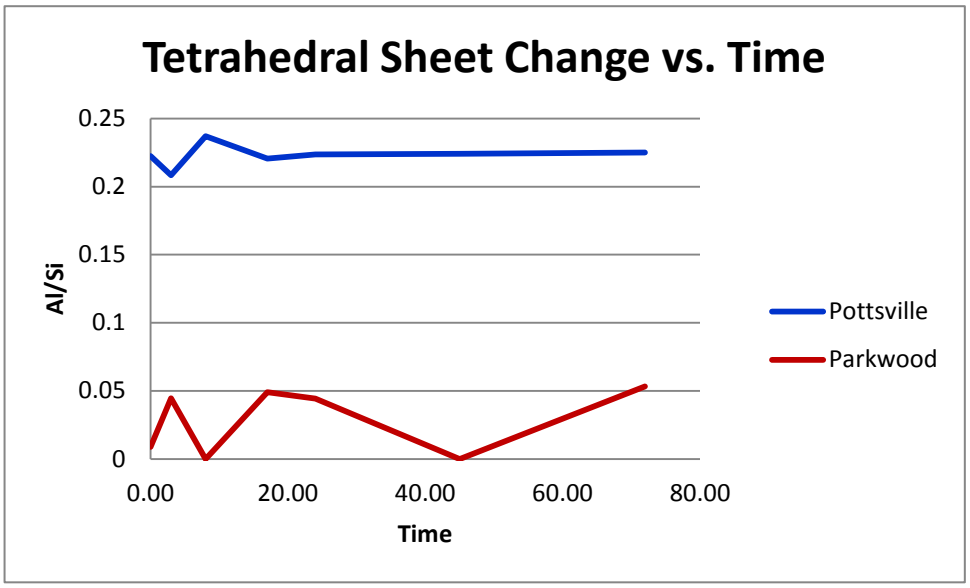

Figure 3-19 Tetrahedral Composition vs. Time

3.4.3 SEM/EDS

SEM images coupled with EDS data have produced a qualitative way of looking at sample change. Pottsville Formation (Figure 3-2020 - Figure 3-222) shows a reduction in aluminosilicates and the appearance of dissolution pits, which are included in the sample exposed to the brine without CO_2 (Figure 3-211 - Figure 3-222).

The Parkwood Formation shows the loss of an Fe-aluminosilicate, possibly Fe-chlorite, through the EDS data in Figure 3-23-Figure 3-25. The Parkwood Formation also shows a loss of Al, K, and Fe with possible precipitation of amorphous silica. Dissolution pits are also present in the Parkwood formation.

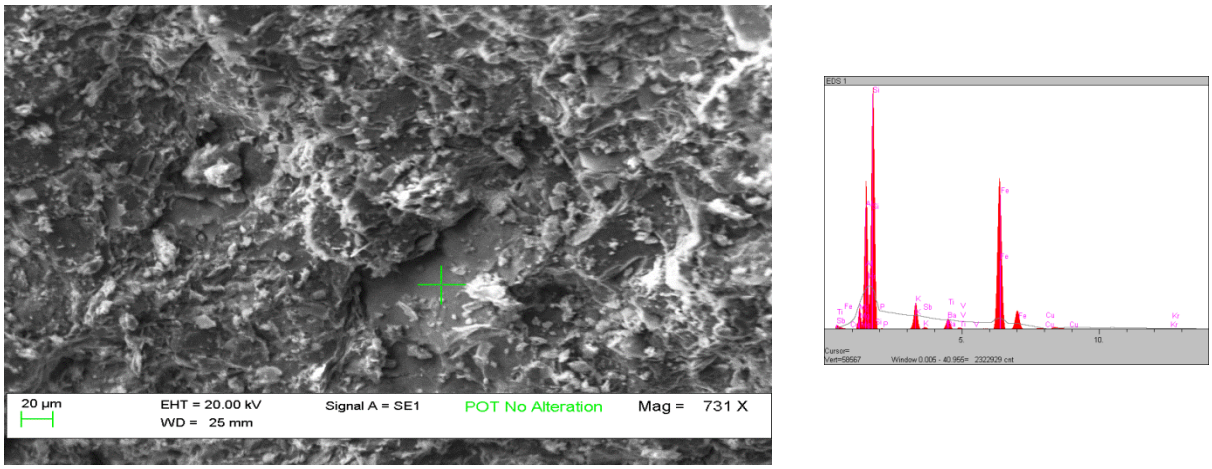

Figure 3-20 SEM image Pottsville Unaltered and EDS

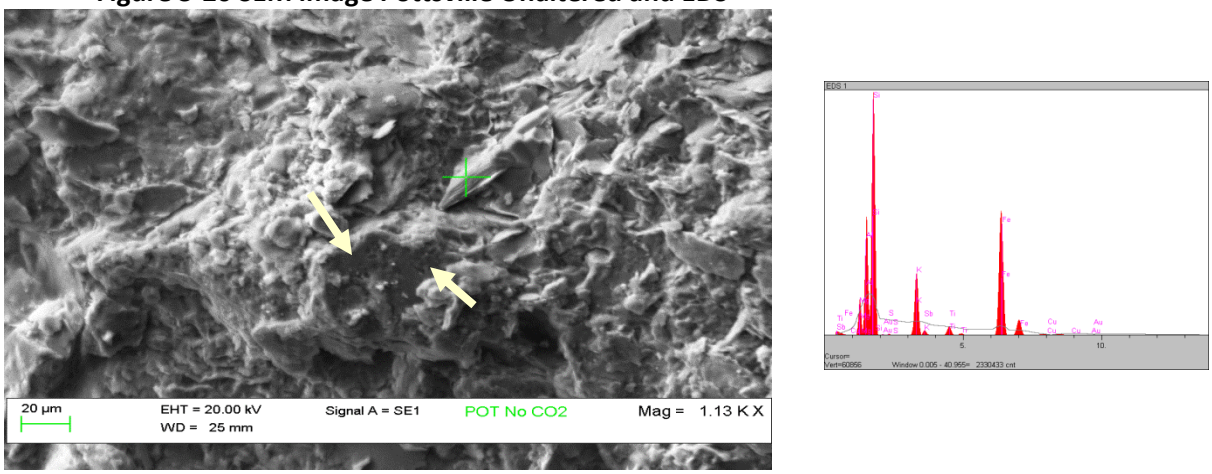

Figure 3-21 Pottsville No CO2 and EDS

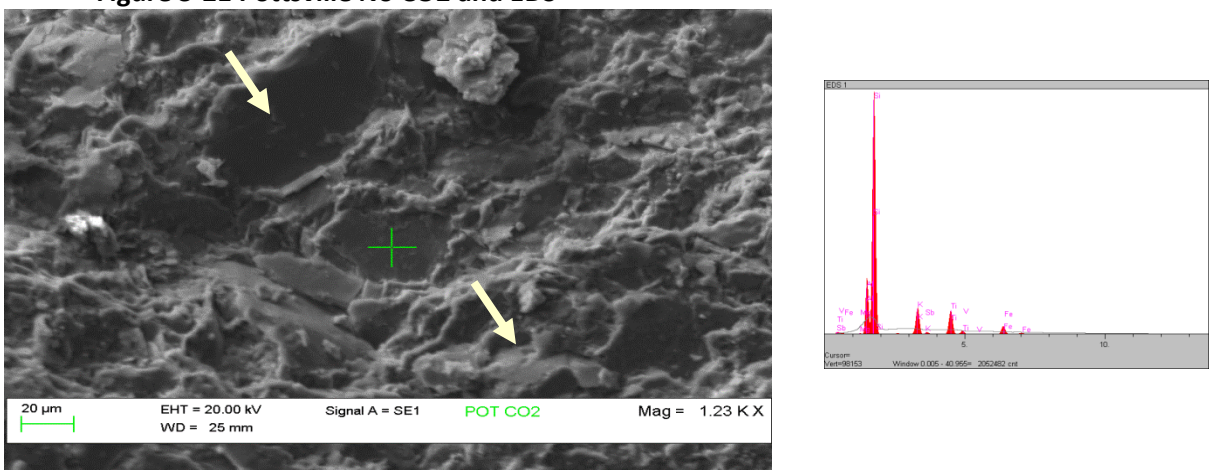

Figure 3-22 SEM Image Pottsville CO2 and EDS

Arrows showing the locations of dissolution pits

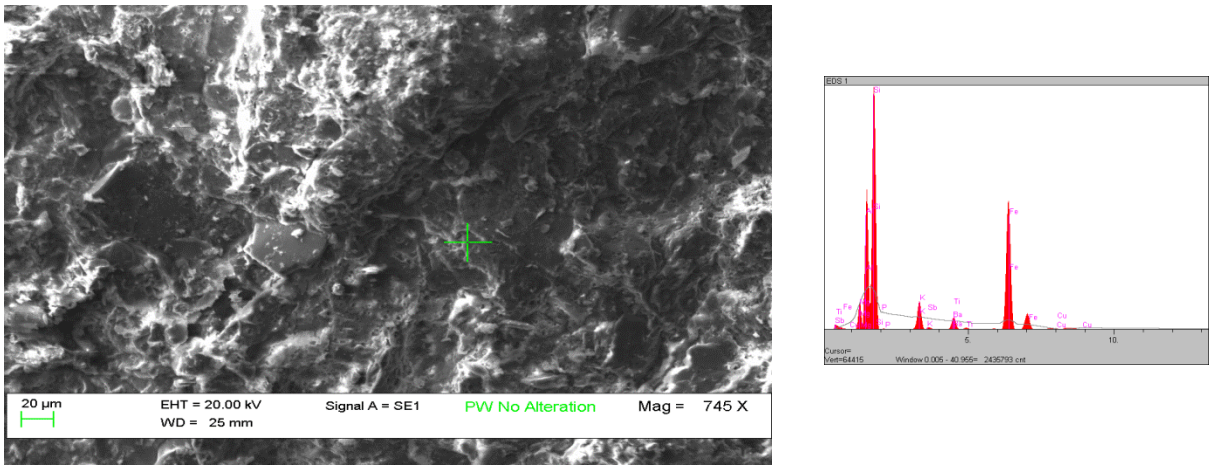

Figure 3-23 SEM Image Parkwood Unaltered and EDS

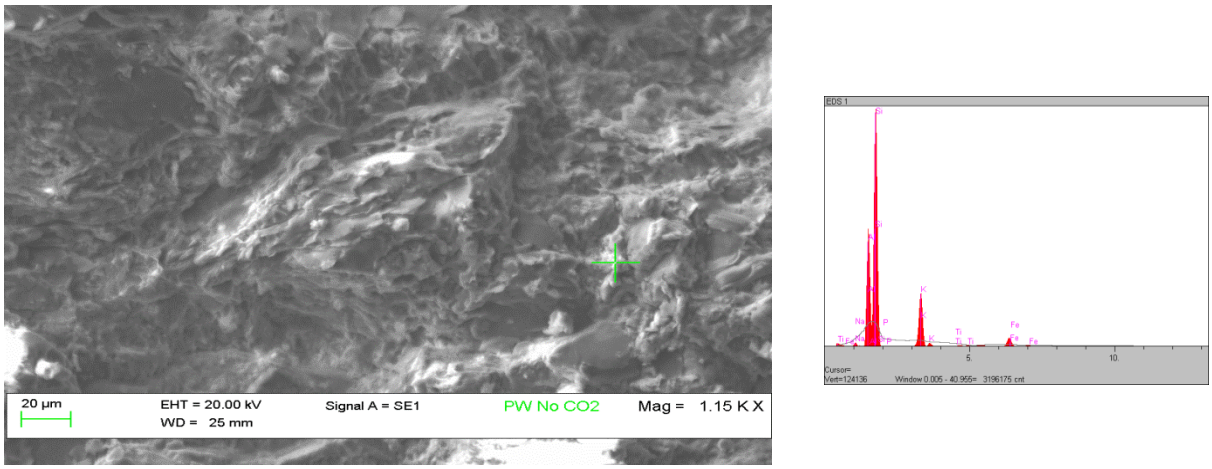

Figure 3-24 SEM Image Parkwood No CO2 and EDS

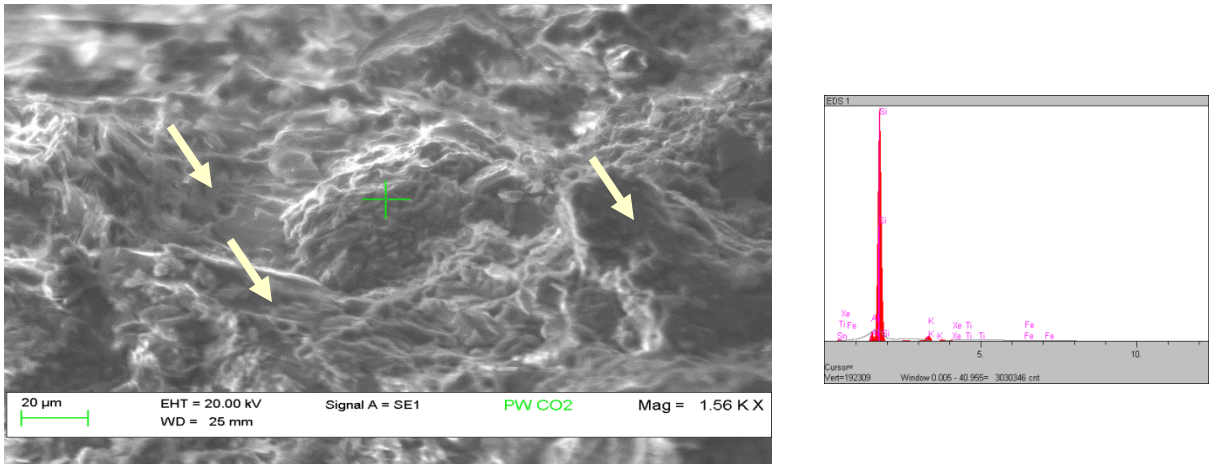

Figure 3-25 SEM Image Parkwood CO2 and EDS
Arrows showing the locations of dissolution pits

4 DISCUSSION

4.1 Mineralogy

The High Score output of the random mount whole rock samples differs from interpretations of clay content from Moore and Reynolds (1997). The identification of 'muscovite' is most likely the identification of the 10Å clay illite. This misidentification is most likely a function of the sample being a 2- or 3-layer polytype of illite with (001) oriented parallel to the cleavage direction where the dissolution of illite aided in its re-precipitation into the (001) orientation and a slight shift towards the end-member, muscovite (Grub *et al.*, 1991). This would occur as the amount of K and Al increased in the sample. Therefore, it is suggested that High Score's classification of 'muscovite' in both the Pottsville and the Parkwood formations is a function of detrital illite composition moving toward its muscovite end-member, and should instead be interpreted as illite. Illite identification is confirmed by XRD clay analysis data.

The identification of 'vermiculite' is also likely incorrect, and is most likely the identification of the 14Å clay chlorite. Analysis was not performed to confirm or deny the validity of the composition of chlorite. However, this interpretation follows the oriented clay mineral interpretation (Moore and Reynolds, 1997). Additional testing, including saturating the sample with formamide to insure the correct identification of chlorite and not kaolinite or halloysite needs to be done (Moore and Reynolds, 1997).

4.2 Fluid Chemistry

The change in fluid chemistry is a strong indicator of dissolution reactions occurring from clay minerals in the experimental procedure. For both potassium and silica, the majority of the dissolution occurred in the early portions of the experiment. This increase in K and Si in the brine can be attributed to the loss of illite into solution which is correlated to K increase in the brine (Almeu *et al.*, 2011). The

molar ratio K:Si of the brine near equilibrium compared to the same molar ratio of the idealized illite formula suggests; however, that illite is first precipitated into the brine, but then, due to the remaining higher concentrations of K in the brine, silica precipitates out, possibly as amorphous silica as suggested by SEM/EDS data.

Minor fluctuations in brine composition could be attributed to minor differences in sample composition stemming from a non-homogeneous mixture of sample creating varying proportions of clay types in each experimental run. Unfortunately, unless known portions of isolated clays were mixed, there would be no way to prevent this from occurring within the parameters of this experimental method. Having an unknown mixture of clay minerals has created, to a degree, ambiguity in the fluid chemistry results.

4.3 Solid Phase Reactions

X-ray diffraction data show both the Pottsville and the Parkwood formations are mostly composed Fe-chlorite, illite, kaolinite, and quartz. With increasing exposure to CO_2 and brine, there is a change in the composition of the clays from both samples that roughly mimic each other, indicating that the change in the clay is not a function of a lack of homogeneity in samples, but instead, a trend in the alteration of clay composition.

In both samples, a decrease in the amount of illite in relation to the amount of Fe-chlorite is indicative of the dissolution of illite. Towards the end of the reaction time, the relative abundance of illite increases again, suggesting the reprecipitation of illite. Illite precipitation has been confirmed in the works of Almeu *et al.* (2011), Credoz *et al.* (2011), Hu *et al.* (2011), Shao *et al.* (2011), and Garcia *et al.* (2012).

XRF data show there is no linear change in the tetrahedral or octahedral layers in relation to time and exposure to supercritical CO_2 and brine. This suggests that congruent dissolution and precipitation reactions dominate the experiment, implying there are not significant clay mineral transformations.

SEM/EDS data also qualitatively confirms the dissolution of mineral surfaces. The Pottsville and the Parkwood Formations show dissolution pits on mineral surfaces. These surfaces are identified as Fe-chlorite because of the Fe content from the EDS data and its correlation to XRD data. This indicates that smectite was dissolving into solution. Silica abundance increases, indicating the precipitation of amorphous silica. Though silica typically dissolves at higher pH and the supercritical CO_2-brine solution is acidic, the clay-brine interface has a higher pH which leads to the dissolution of silica (Thomson, 1959). Therefore it is hypothesized that the silica is then transported to regions of lower pH, where it is deposited.

These results illustrate the need for further study. If dissolution reactions are occurring in geological CO_2 sequestration conditions, this will directly affect the permeability of the reservoir and the reservoir seal. Precipitation reactions could restrict the injectivity of a formation by decreasing pore throat diameters. Therefore, it is essential to fully understand the geochemical effects of the brine-rock-CO_2 system with respect to time so as to make long-term predictions about the viability of a formation.

5 Future Work

To improve upon the research done in this study, more extensive XRD analytical techniques need to be applied. To verify the presence of chlorite, samples should be heated to 550˚C for one hour to cause dehydroxylation of the hydroxide sheet and shift the (001) reflection from about 6.3 to 6.4 2Θ and reduce the (002-004) reflections. Air dried sample diffractograms also need to be compared to compare to all forms of treatment. To verify whether the samples contain vermiculite or chlorite with Fe substitution, a treatment of k-saturation is necessary.

Observing a single sample throughout the duration of the experiment is crucial to understanding the effects of geologic CO_2 sequestration conditions. This will also help SEM analysis to move from a

qualitative analysis to a quantitative analysis. Using the same sample will show what happens to individual crystals and the matrix with time and exposure to CO_2.

To better understand what actually happens to clay minerals, individual clays must be modeled in water, brine, and brine plus CO_2. This will allow for accurate assessments about what is occurring to each clay and help to make accurate predictions about what is occurring to the whole rock in geologic CO_2 sequestration conditions.

A full suite of AA or inductively coupled plasma mass spectrometry (ICP-MS) data needs to be collected to quickly and accurately assess what elements are moving into and out of the clay system. This must be performed on samples that have been reacted with water, brine, and brine plus CO_2 to show how brine chemistry is affected by the brine composition as well as the addition of CO_2 in conjunction with the clay under observation. The data produced would inform the researcher about when the rock-brine-CO_2 system stabilized. In conjunction with other data, like XRF, predictions about the clay fraction of a whole rock can be made.

The biggest question left to be answered in the field of geological CO_2 sequestration is how the permeability of the reservoir rock or the caprock of the target formation is affected by the rock-brine-CO_2 system. To understand this, it is proposed that a new series of tests be run. First, a flow-through test must be performed on a section of core or plug to determine its initial permeability. Then the point of stabilization of the rock-brine-CO_2 system must be determined through batch reactions and AA data. After the rock has stabilized, another flow-through test must be performed to determine the change in permeability. This would allow for an accurate quantification of how the geologic sequestration of CO_2 will affect the permeability, hence storativity, of a target reservoir and its caprock.

6 CONCLUSIONS

- This experiment has shown that the clay fractions of caprocks are affected by supercritical CO_2 introduction to the simulated pore fluids.
- The major clays identified using XRD are Fe-chlorite, illite, smectite and kaolinite.
- Reactions of the mixture of clay-brine-CO_2 are documented by changes in the aqueous chemistry relative to the starting brine.
- The brine composition stabilized within 70 hours, indicating the clay-brine-CO_2 system will equilibrate at some point, which is determined by the composition of the clay-brine system.
- Dissolution of the clay minerals was illustrated by XRD and SEM/EDS results.
- SEM/EDS results also suggest the precipitation of silicate minerals.
- XRF data suggests congruent dissolution precipitation reactions as the main catalyst for change in the clay system since there is no major change recorded in the structural formula of the tetrahedral or octahedral structure of either clay.
- While each method of observing the changes in clay mineralogy indicated some change, or lack thereof, the observations between methods were not totally parallel because each method observes the sample on a different scale.
- The current data calls for further research into the long-term stability of all potential formations for geologic CO_2 sequestration caprocks as well as their reservoirs

REFERENCES

Allinson, W. G., Nguyen, D.N., Bradshaw, J., 2003, The Economics of Geological Storage of CO_2 in Australia: APPEA Journal, p. 623.

Almeu, B. L., Aagaard, P., Munz, I.A., Skurtveit, E., 2011, Caprock interaction with CO_2: A laboratory study of reactivity of shale with supercritical CO_2 and brine: Applied Geochemistry, v. 26, p. 1975-1989.

Aydin, G., Karakurt, K, Aydiner, K., 2010, Evaluation of geologic storage options of CO_2: Applicability, cost, storage capacity and safety: Energy Policy, v. 38, p. 5072-5080.

Billets, S., 2006, XRF Technologies for Measuring Trace Elements in Soil and Sediment: EPA Innovative Technology Verification Report.

Bock, B., Rhudy, R, Herzog, H., Klett, M., Davidson, J., Della Torre Ugarte, D., Simbec, D., 2003, Economic Evaluation of CO_2 Storage and Sink Options: DOE Research Report.

Chadwick, R. A., Zweigel,T. Gregersen, U., Kirby, G.A. Holloway, S., Johannessen, P.N., 2004, Geological reservoir characterization of a CO_2 storage site: The Utsira Sand, Sleipner, northern North Sea: Energy, v. 29, p. 1371-1381.

Credoz, A., Vildstein, O., Jullien, M., Raynal, J., Trotignon, L., Pokrovsky,O., 2011, Mixed layer illite smectitie reactivity in acidified solutions: implications for clayey caprock stability in CO_2 geological storage: Applied Clay Science, v. 53, p. 402-408.

Demko, T. M., Gastaldo, R.A., 1992, Paludal environments of the Mary Lee coal zone, Pottsville Formation, Alabama: stacked clastic swamps and peat mires: International Journal of Coal Geology, v. 20, p. 23-47.

Deocampo, D. M., Ashley, G.M., 1999, Siliceous islands in a carbonate sea: modern and Pleistocene spring-fed wetlands in Ngorongoro crater and Oldupai Gorge, Tanzania: Journal of Sedimentary Research, v. 69, no. 5, p. 974-979.

Deocampo, D. M., Behrensmeyer, A.K., and Potts, R., 2010, Ultrafine clay minerals of the Pleistocene Olorgesailie Formation, Southern Kenya Rift: Digenesis and Paleoenvironments of Early Hominins: Clays and Clay Minerals, v. 58, p. 293-309.

Deocapmo, D., 2004, Authigenic clays in East Africa: Regional trends and paleolimnology at the Plio-Pleistocene boundary, Olduavi Gorge, Tanzania: Journal of Paleolimnology, v. 31, p. 1-9.

Drever, J. I., 1997, The geochemistry of natural waters: N.J., Prentice Hall p. 437.

Duan, Z., Sun, R., 2003, An improved model calculating CO_2 solubility in pure water and aqueous NaCl solutions from 273 to 533 K and from 0 to 2000 bar: Chemical Geology, v. 193, p. 257–271.

Gale, J. a. D., D., 2003, Transmission of CO_2: Safety and economic considerations, Sixth International Conference on Greenhouse Gas Control Technologies, Kyoto, Volume 1: Pergamon, Amster-dam, p. 517–522.

Garcia, D. J., Shao, H., Hu, Y., Ray, J. R., Jun, Y., 2012, Supercritical CO_2-brine induced dissolution, swelling, and secondary mineral formation on phlogopite surfaces at 75-90 C and 75 atm: Energy and Environmental Science, v. 5, p. 5758-5767.

Gasda, S. E., Bachu, S., Celia, M.A., 2004, he potential for CO_2 leakage from storage sites in geological media: analysis of well distribution in mature sedimentary basins: Environmental Geology, v. 46, p. 707–720.

Gaus, I., 2010, Role and impact of CO_2-rock interactions during CO_2 storage in sedimentary rocks: International Journal of Greenhouse Gas Control, v. 4, p. 73-89.

Gaus, I., Azaroual, M., Czernichowski-Lauriol, I., 2005, Reactive transport modeling of the impact of CO_2 injection on the clayey cap rock at Sleipner (North Sea): Chemical Geology, v. 217, p. 319-337.

Giammar, D. E., Bruant, R.G., Peters, C.A., 2005, Forsterite dissolution and magnesite precipitation at conditions relevant for deep saline aquifer storage and sequestration of carbon dioxide: Chemical Geology, v. 217, p. 257-276.

Grub, S. B., Peacor, D.R., Jiang, W., 1991, Transmission electron microscope observations of illite polytypism: Clays and Clay Minerals, v. 39, p. 540-550.

Hendricks, C., Graus, W., van Bergen, F., 2002, Global Carbon Dioxide Storage Potential and Costs: Ecofys & The Netherland Institute of Applied Geoscience TNO.

Hewitt, J. L., 1984, Geological overview, coal, and coalbed methane resources of the Warrior Basin – Alabama and Mississippi, *in* Rightmire, C. T., Eddy, G.E., Kirr, J.N., ed., Coalbed Methane Resources of the United States, Volume 17: OK, Studies in Geology series: Association of Petroleum Geologists, p. 73-104.

Horn, F. L., 1982, Control of Carbon Dioxide Emissions from a Power Plant (and Use Enhanced Oil Recovery), Fuel, Volume 61, p. 415-422.

Hu, Y., Ray, J. R., Jun, Y., 2011, Biotite-brine interactions under acidic hydrothermal conditions: fibrous illite goethite, and kaolinite formation and biotite surface cracking: Environmental Science and Technology, v. 45, p. 6175-6180.

IPCC, 2001, Climate Change 2011: The Scientific Basis, New York, Cambridge University Press, 786 p.:

Jenkins, R., Gould, R. W., 1995, Quantitative X-Ray Spectrometry, New York, Marcel Dekker, Inc. , Practical Spectroscopy.

Kumar, A., Datta-Gupta, A., Shekhar,R., Gibson, R. L., 2008, Modeling Time Lapse Seismic Monitor-ing of CO_2 Sequestration in Hydrocarbon Reservoirs Including Compositional and Geochemical Effects: Petroleum Science and Technology, v. 26, p. 887-911.

LaTour, T. E., 1989, Analysis of rocks using X-ray fluorescence spectrometry: Rigaku Journal, v. 6, p. 3-9.

Liu, F., Lu, P., Griffith, C., Hedges,W., Soong, Y., Hellevang, H., Zhu, C., 2012, CO_2 brine-caprock interaction: reactivity experiments on eau Claire shale and a review of relevant literature: International Journal of Greenhouse Gas Control, v. 7, p. 153-167.

Maikala, R. V., 2010, Modified Beer's Law – historical perspectives and relevance in near-infrared monitoring of optical properties of human tissue: International Journal of Industrial Ergonomics, v. 40, p. 125-134.

Marchetti, C., 1977, On Geo-engineering and the CO_2 problem: Climate Change, v. 1, p. 59–68.

Massarotto, P., Golding, S.D., Bae, J.-S., Iyer, R., Rudolph, V., 2010, Changes in reservoir properties from injection of supercritical CO2 into coal seams — A laboratory study: International Journal of Coal Geology, v. 82, p. 269-279.

Metz, B., 2005, IPCC Special Report on Carbon Dioxide Capture and Storage., New York, Cambridge University Press for the Intergovernmental Panel on Climate Change.

Oldenburg, C. M., Unger, A.J., 2003, On leakage and seepage from geologic carbon sequestration sites: unsaturated zone attenuation: Vadose Zone Journal, v. 2, p. 287–296.

Pashin, J. C., 1991a, Defining the Supercritical Phase Window for CO_2 in Coalbed Methane Reser-voirs of the Black Warrior Basin: Implications for CO_2 Sequestration and Enhanced Coalbed Methane Recovery, Alabama Geol. Survey, p. 12.

-, 1991b, Regional analysis of the Black Creek-Cobb coalbed-methane target interval, Black Warrior Basin, Alabama, Energy and Coastal Geology Division, Geological Survey of Alabama.

-, 1994, Cycles and stacking patterns in carboniferous rocks of the Black Warrior foreland basin: ransactions of the Gulf Coast Association of Geological Societies, v. 44, p. 555-563.

-, 2004, Cyclothems of the Black Warrior Basin in Alabama: eustatic snapshots of f forel-and basin tectonism: American Association of Petroleum Geology Stud. Geol., v. 51, p. 99-217.

-, Gas shale potential of Alabama, *in* Proceedings 2008 International Coalbed and Shale Gas Symposium, University of Alabama, College of Continuing Studies, 2008, p. 13.

Pashin, J. C., 2007. Hydrodynamics of coalbed methane reservoirs in the Black Warrior Basin: Key to understanding reservoir performance and environmental issues. Applied Geochemistry,

22:2257-2272., 2007, Hydrodynamics of coalbed methane reservoirs in the Black Warrior Basin: Key to understanding reservoir performance and environmental issues: Applied Geochemistry, v. 22, p. 2257-2272.

Pashin, J. C., Gastaldo, R.A., 2009. Carboniferous of the Black Warrior Basin, in Greb, S.F., Chestnut, D.R., eds., Carboniferous Geology and Biostratigraphy of the Appalachian Basin: Kentucky Geological Survey, pp. 10-21., 2009, Carboniferous of the Black Warrior Basin, *in* Greb, S. F., Chestnut, D.R., ed., Carboniferous Geology and Biostratigraphy of the Appalachian Basin, Kentucky Geological Survey, p. 10-21.

Reynolds, M. a., 1997, X-ray diffraction and the identification and analysis of clay minerals, New York, Oxford University Press.

Shao, H., Ray, J.R., Jun, Y., 2010, Dissolution and precipitation of clay mineral under geological CO_2 sequestration conditions: CO_2 – brine-phlogopite interactions: Environmental Science and Technology, v. 44, p. 5999-6005.

-, 2011a, Effects of organic ligands on supercritical CO2-induced phlogopite dissolution and secondary mineral formation: Chemical Geology, v. 290, p. 121-132.

-, 2011b, Effects of salinity and the extent of water on supercritical CO_2 induced phlogopite dissolution and secondary mineral formation: Environmental Science and Technology, v. 45, p. 1737-1743.

Siddique, Q., Separation of Gases, *in* Proceedings Proceedings of 5th Priestley Conference, London, 1990, Roy. Soc. Chem., p. 329.

Thomas, W. A., 1977, Evolution of the Appalachian-Ouachita salients and recesses from reentrants and promontories in the continental margin: American Journal of Science, v. 277, p. 1233-1278.

-, 1988, The Black Warrior basin, *in* Sloss, L. L., ed., Sedimentary cover – North American Craton , U.S., Volume D-2, Geological Society of America, The Geology of North America, p. 471-492.

-, 1997, Evolution of the Appalachian-Ouachita salient and recesses from reentrants and promontories in the continental margin: American Journal of Science, v. 277, p. 1233-1278.

Thomson, A., 1959, Pressure solution and porosity, *in* Proceedings Silica in sediments – a symposium 1959, Volume 7, Society of Economic Paleontologists and Mineralogists Special Publication, p. 92-110.

Iowa State University, 2009, Understanding how the SEM works and how to use it on a college level, http://mse.iastate.edu/microscopy/college.html.

Wigand, M., Carey, J.W., Shutt, H., Spangenberg, E., Erzinger, J., 2008, Geochemical effects of CO_2 sequestration in sandstones under simulated in situ conditions of deep saline aquifers: Applied Geochemistry, v. 23, no. 2735-2745.

Zeman, F., 2007. Energy and material balance of CO¬2 capture from ambient air. Environmental Science & Technology, 41:7558-7563, 2007, Energy and material balance of CO_2 capture from ambient air: Environmental Science & Technology, v. 41, p. 7558-7563.

http://www.eia.gov/oiaf/1605/ggrpt/carbon.html#total.

http://www.netl.doe.gov/publications/proceedings/10/rascp/Alabama_Clark.pdf.

http://www.purdue.edu/rem/rs/sem.htm#2.

APPENDICES

Appendix A - Abbreviations

AA	atomic absorption
Al	Aluminum
Au	Gold
CCS	carbon capture and storage
H_2CO_3	carbonic acid
CDM	clean development mechanism credits
K	Potassium
MMV	monitoring, managing and verification
Pt	Platinum
Si	Silica
CH_3COONa	Sodium Acetate
NaCl	Sodium Chloride
STP	standard temperature and pressure
XRD	X-Ray diffraction
XRF	X-Ray fluorescence

Appendix B - Batch Reaction Pressure Calculations

Pressure Calculations

Showing the pressure inside each reaction based on solubility of CO_2, volume clay, volume brine.

Sample	Time hrs.	Vol Brine mL	Mass Sample g	Mass CO2 g	mole CO2	Vol Sample	Temp. Reaction C	Temp. Reaction K	Volume Void mL	Pressure in atm	Pressure in PSI	Pressure in bar	mwCO2 in g/mol	Solubility CO2 363K& 100bar molCO2/kgH2O	Mass Water (Kg)	mol CO2 into solution	mol CO2 into head-space
Pot_Cube_Brine_NoCO2	165	18	2.599	1.500	0.034	0.981	90.000	363.000	4.019	143.083	2102.736	144.979	44.000	0.822	0.018	0.015	0.019
PW_Cube_Brine_NoCO2	167	18	2.491	1.500	0.034	0.940	90.000	363.000	4.060	141.647	2081.628	143.523	44.000	0.822	0.018	0.015	0.019
Pot_Cube_CO2	159	18	2.590	1.500	0.034	0.977	90.000	363.000	4.023	142.962	2100.961	144.856	44.000	0.822	0.018	0.015	0.019
PW_Cube_CO2	165.5	18	2.580	1.500	0.034	0.974	90.000	363.000	4.026	142.828	2098.991	144.720	44.000	0.822	0.018	0.015	0.019
Pot_Clay_CO2_8	8	18	0.407	1.500	0.034	0.154	90.000	363.000	4.846	118.662	1743.848	120.234	44.000	0.822	0.018	0.015	0.019
Pot_Clay_CO2_17	17	18	0.403	1.500	0.034	0.152	90.000	363.000	4.848	118.625	1743.305	120.197	44.000	0.822	0.018	0.015	0.019
Pot_Clay_CO2_24	24	18	0.409	1.500	0.034	0.154	90.000	363.000	4.846	118.681	1744.120	120.253	44.000	0.822	0.018	0.015	0.019
Pot_Clay_CO2_45	45	18	0.402	1.500	0.034	0.152	90.000	363.000	4.848	118.616	1743.169	120.187	44.000	0.822	0.018	0.015	0.019
Pot_Clay_CO2_70	70	18	0.408	1.500	0.034	0.154	90.000	363.000	4.846	118.671	1743.984	120.243	44.000	0.822	0.018	0.015	0.019
PW_Clay_CO2_3	3	18	0.407	1.500	0.034	0.154	90.000	363.000	4.846	118.662	1743.848	120.234	44.000	0.822	0.018	0.015	0.019
PW_Clay_CO2_8	8	18	0.408	1.500	0.034	0.154	90.000	363.000	4.846	118.671	1743.984	120.243	44.000	0.822	0.018	0.015	0.019
PW_Clay_CO2_17	17	18	0.410	1.500	0.034	0.155	90.000	363.000	4.845	118.690	1744.255	120.262	44.000	0.822	0.018	0.015	0.019
PW_Clay_CO2_24	24	18	0.405	1.500	0.034	0.153	90.000	363.000	4.847	118.644	1743.576	120.215	44.000	0.822	0.018	0.015	0.019
PW_Clay_CO2_45	45	18	0.404	1.500	0.034	0.152	90.000	363.000	4.848	118.634	1743.441	120.206	44.000	0.822	0.018	0.015	0.019
PW_Clay_CO2_70	70	18	0.408	1.500	0.034	0.154	90.000	363.000	4.846	118.671	1743.984	120.243	44.000	0.822	0.018	0.015	0.019
Pot_Na_Clay_CO2_3	3		0.548	1.500	0.034	0.207	90.000	363.000	4.793	119.979	1763.206	121.569	44.000	0.822	0.018	0.015	0.019
Pot_Na_Clay_CO2_8	8	18	0.550	1.500	0.034	0.208	90.000	363.000	4.792	119.998	1763.483	121.588	44.000	0.822	0.018	0.015	0.019
Pot_Na_Clay_CO2_17	17	18	0.550	1.500	0.034	0.208	90.000	363.000	4.792	119.998	1763.483	121.588	44.000	0.822	0.018	0.015	0.019
Pot_Na_Clay_CO2_24	24	18	0.550	1.500	0.034	0.208	90.000	363.000	4.792	119.998	1763.483	121.588	44.000	0.822	0.018	0.015	0.019
Pot_Na_Clay_CO2_45	45	18	0.544	1.500	0.034	0.205	90.000	363.000	4.795	119.942	1762.651	121.530	44.000	0.822	0.018	0.015	0.019
Pot_Na_Clay_CO2_70	70	18	0.550	1.500	0.034	0.208	90.000	363.000	4.792	119.998	1763.483	121.588	44.000	0.822	0.018	0.015	0.019
PW_Na_Clay_CO2_3	3	18	0.550	1.500	0.034	0.208	90.000	363.000	4.792	119.998	1763.483	121.588	44.000	0.822	0.018	0.015	0.019
PW_Na_Clay_CO2_8	8	18	0.551	1.500	0.034	0.208	90.000	363.000	4.792	120.008	1763.622	121.597	44.000	0.822	0.018	0.015	0.019
PW_Na_Clay_CO2_17	17	18	0.551	1.500	0.034	0.208	90.000	363.000	4.792	120.008	1763.622	121.597	44.000	0.822	0.018	0.015	0.019
PW_Na_Clay_CO2_24	24	18	0.551	1.500	0.034	0.208	90.000	363.000	4.792	120.008	1763.622	121.597	44.000	0.822	0.018	0.015	0.019
PW_Na_Clay_CO2_45	45	18	0.550	1.500	0.034	0.208	90.000	363.000	4.792	119.998	1763.483	121.588	44.000	0.822	0.018	0.015	0.019
PW_Na_Clay_CO2_70	70	18	0.550	1.500	0.034	0.208	90.000	363.000	4.792	119.998	1763.483	121.588	44.000	0.822	0.018	0.015	0.019

Appendix C - Phillips X-Ray Diffractometer Data

Peak areas for data collected from the Philips X-ray Diffractometer were determined by hand instead of using software. The intensity at every 0.02 Θ measurement was subtracted from the previous intensity count. This was done so that individual peaks could be observed by the series of positive and negative differences in the results. Once the peak was determined, the area under the peak was calculated accounting for the difference between the intensity at the beginning and end of the peak.

Peak area calculations were based on a definite integral to calculate the area under a curve using the upper and lower sums method common to univariate calculus.

The *left sum* (analogous to the lower sum) is given by:

$$Lp(P) = \sum_{a}^{b-1} \Delta\theta \cdot p_i = \sum_{a}^{b-1} (0.02) \cdot p_i = 0.02 \sum_{a}^{b-1} p_i$$

Left Sum Calculation

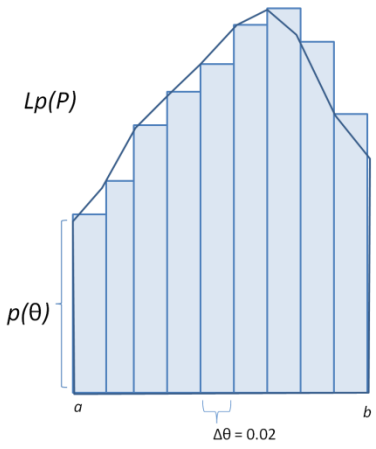

Left Sum Example

Where a, b are the left and right limits of integration, Δθ is the constant 0.02 (as per XRD steps) for the width of the partitions, and $p_i = p(\theta)$ is the diffraction measurement at each θ in the domain of integration.

The *right sum* (analogous to the upper sum) is given by:

$$Rp(P) = 0.02 \sum_{a+1}^{b} p_i$$

Right Sum Calculation

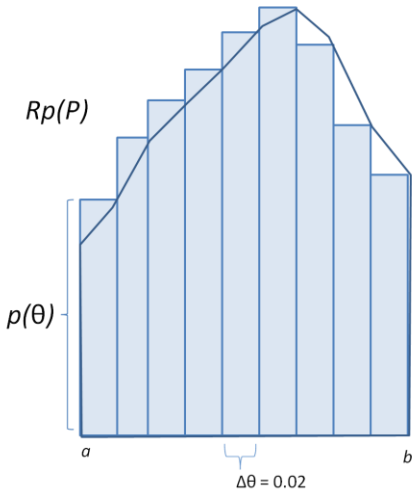

Right Sum Example

Then the average of the left and right sums approximates (precisely) the area under the entire curve.

$$\int_a^b p(\theta)d\theta \cong \frac{Lp(P) + Rp(P)}{2} = \frac{0.02\sum_a^{b-1} p_i + 0.02\sum_{a+1}^{b} p_i}{2} = 0.01\left(\sum_a^{b-1} p_i + \sum_{a+1}^{b} p_i\right)$$

Area Under Curve Calculation

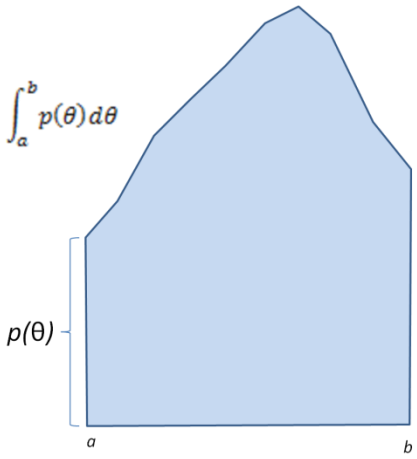

Area under the Curve Example

The excess area under the curve must be taken into consideration. The excess area is calculated by averaging the areas of the small and large rectangles given by the length of the base by $p(a)$ and the length of the base by $p(b)$.

It is given by the following formula:

$$A_{excess} = \frac{(b-a)p(a) + (b-a)p(b)}{2} = (b-a)\frac{p(a)+p(b)}{2}$$

Excess Area Calculation

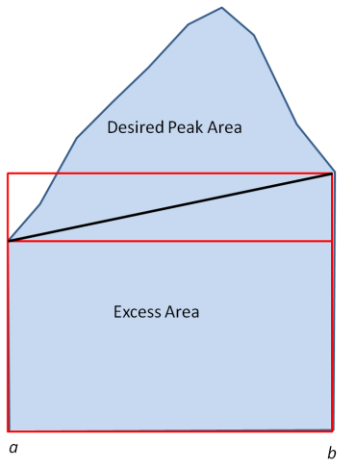

Excess Area Example

Then the final formula for peak area is as follows:

$$A_{peak} = \int_a^b p(\theta)d\theta \; - A_{excess} = 0.01\left(\sum_{a}^{b-1} p_i + \sum_{a+1}^{b} p_i\right) - \; (b-a)\frac{p(a)+p(b)}{2}$$

Final Peak Area Calculation

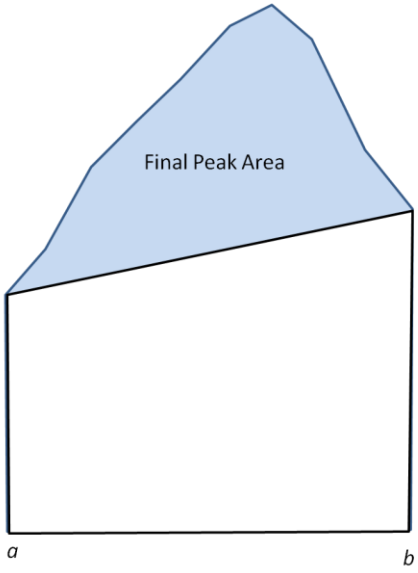

Final Peak Area

This formula was executed in Microsoft Excel to calculate the peak areas.

Comparison of Phillips and PANalytical data

Data from the Phillips XRD and from the PANalytical XRD are different, even though the same samples were analyzed. An example, Pottsville_3hr shows a different reading based on the diffracto-grams present. Aside from changes in peak locations, the smectite (001) peak was not present in the Phillips diffractogram, nor was the illite/smectite (002/003) peak, the illite (002) peak, or the quartz (022) peak.

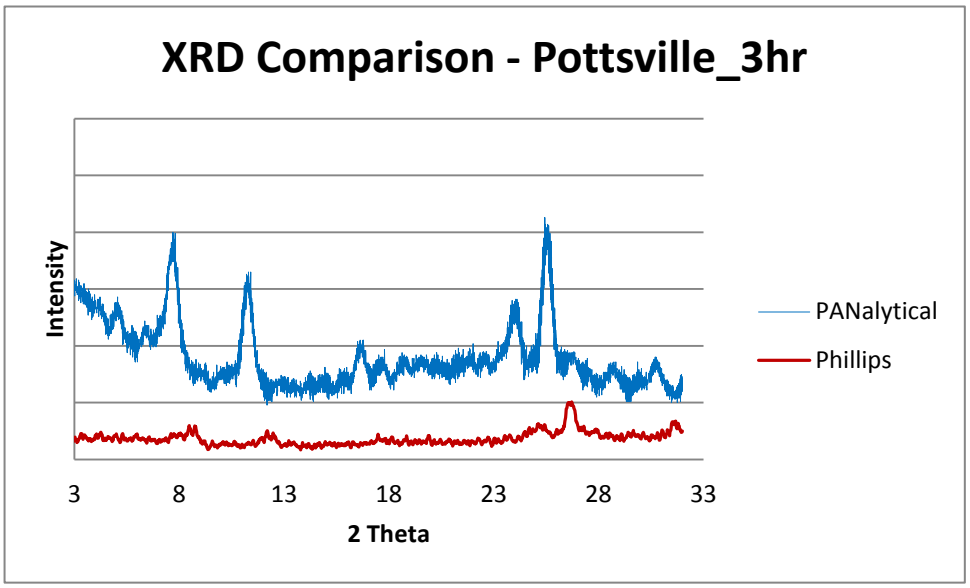

Diffractometer Comparison of Clay Fraction

The random mounted whole rock analysis also showed variations in peak location, presence, and intensity.

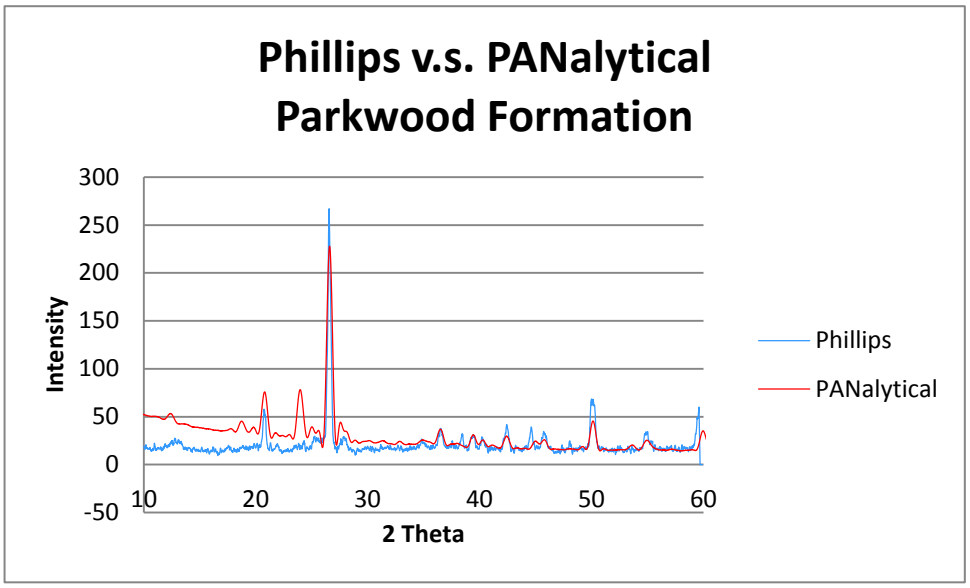

Diffractometer Comparison Random Mounted Whole Rock

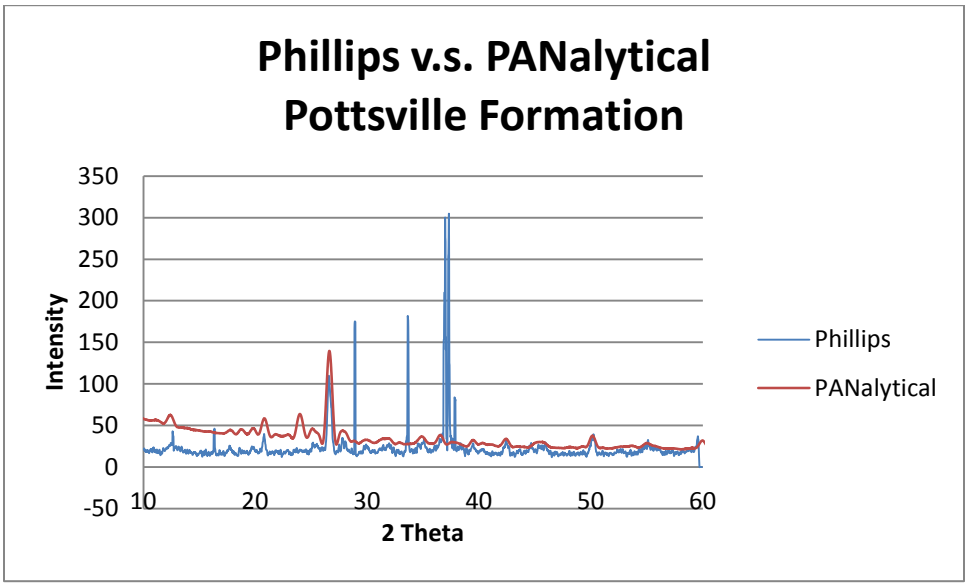

Diffractometer Comparison Random Mounted Whole Rock

When comparing the relative abundances of the Illite (001) peak and the Kaolinite (001) peak, the results were almost the inverse of each other. The integrated area under the curve was used to calculate peak area for the Phillips XRD, High Score for the PANalytical.

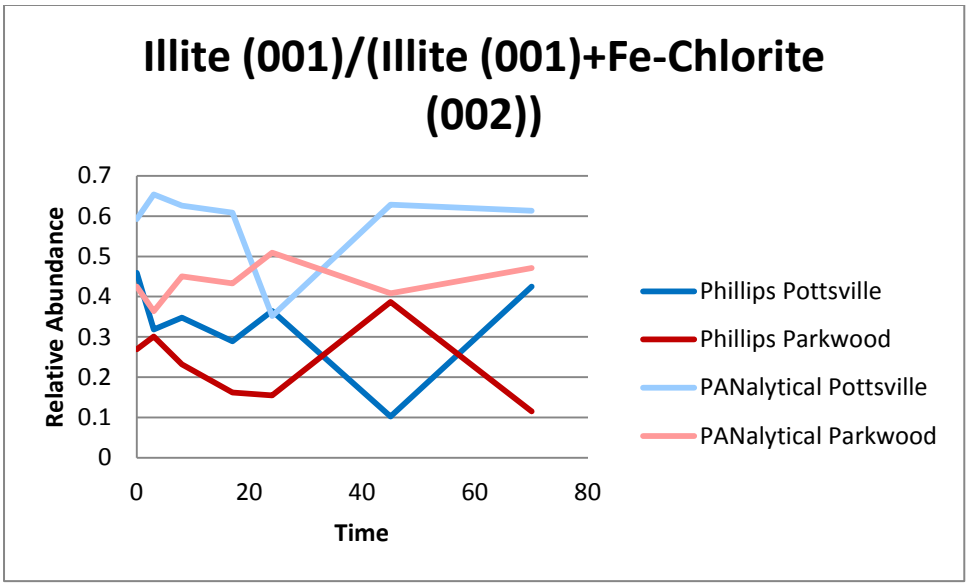

Phillips XRD vs. PANalytical XRD

Appendix D - PANalytical X-Ray Diffraction Data

Pottsville Whole Rock PANalytical High Score Analysis

Muscovite represents the 10 Å clay illite
Vermiculite represents the 14 Å clay Chlorite

Peak #	°2Theta	Intensity	d-Spacing [Å]	Rel. Int. [%]	High Score Prediction
1	**7.9066**	252.9	11.18225	2.28	N/A
2	**8.7801**	1202.62	10.07153	10.84	Muscovite
3	**11.2214**	242.77	7.8853	2.19	Vermiculite
4	**12.4395**	1231.73	7.11579	11.1	Vermiculite
5	**17.7182**	458.74	5.00591	4.14	Muscovite
6	**18.7329**	589.32	4.737	5.31	Vermiculite
7	**19.7817**	758.68	4.48814	6.84	Muscovite
8	**20.8163**	2062.86	4.26736	18.6	Quartz
9	**21.7789**	245.2	4.08087	2.21	Muscovite
10	**23.0358**	299.12	3.86098	2.7	Muscovite
11	**23.9581**	2975.76	3.7144	26.83	Muscovite
12	**25.0272**	1408.7	3.5581	12.7	Muscovite
13	**25.7211**	793.88	3.46365	7.16	Muscovite
14	**26.6119**	11092.69	3.34971	100	Quartz
15	**27.5487**	1141.4	3.23788	10.29	Muscovite
16	**28.0733**	1243.71	3.17856	11.21	Muscovite
17	**28.9213**	154.1	3.08726	1.39	Muscovite
18	**29.8328**	308.51	2.99498	2.78	Muscovite
19	**31.2601**	463.08	2.86142	4.17	Muscovite
20	**32.032**	558.43	2.7942	5.03	Muscovite
21	**32.8556**	163.51	2.72602	1.47	Vermiculite
22	**34.9819**	805.96	2.56504	7.27	Muscovite
23	**36.4981**	1068.91	2.46189	9.64	Quartz
24	**37.4737**	303.6	2.40001	2.74	Muscovite
25	**39.4552**	728	2.28393	6.56	Quartz
26	**40.3119**	344.03	2.23735	3.1	Quartz
27	**41.1275**	152.72	2.19484	1.38	Muscovite
28	**42.4226**	896.74	2.13079	8.08	Quartz
29	**45.0137**	507.58	2.01397	4.58	Muscovite
30	**45.9095**	504.58	1.97674	4.55	Quartz
31	**48.0932**	126.62	1.89196	1.14	Muscovite
32	**50.1596**	1462.18	1.81876	13.18	Quartz
33	**52.822**	129.73	1.73319	1.17	Muscovite
34	**53.6487**	189.36	1.70842	1.71	Muscovite
35	**54.935**	526.92	1.67142	4.75	Muscovite
36	**59.9515**	879.99	1.54301	7.93	Quartz
37	**60.8368**	321.19	1.52266	2.9	Muscovite
38	**61.6581**	366.74	1.50433	3.31	Muscovite
39	**64.0351**	143.24	1.45411	1.29	Muscovite
40	**65.4107**	151.18	1.42682	1.36	Muscovite
41	**68.1118**	1182.6	1.37667	10.66	Quartz
42	**69.2263**	153.31	1.35721	1.38	Muscovite

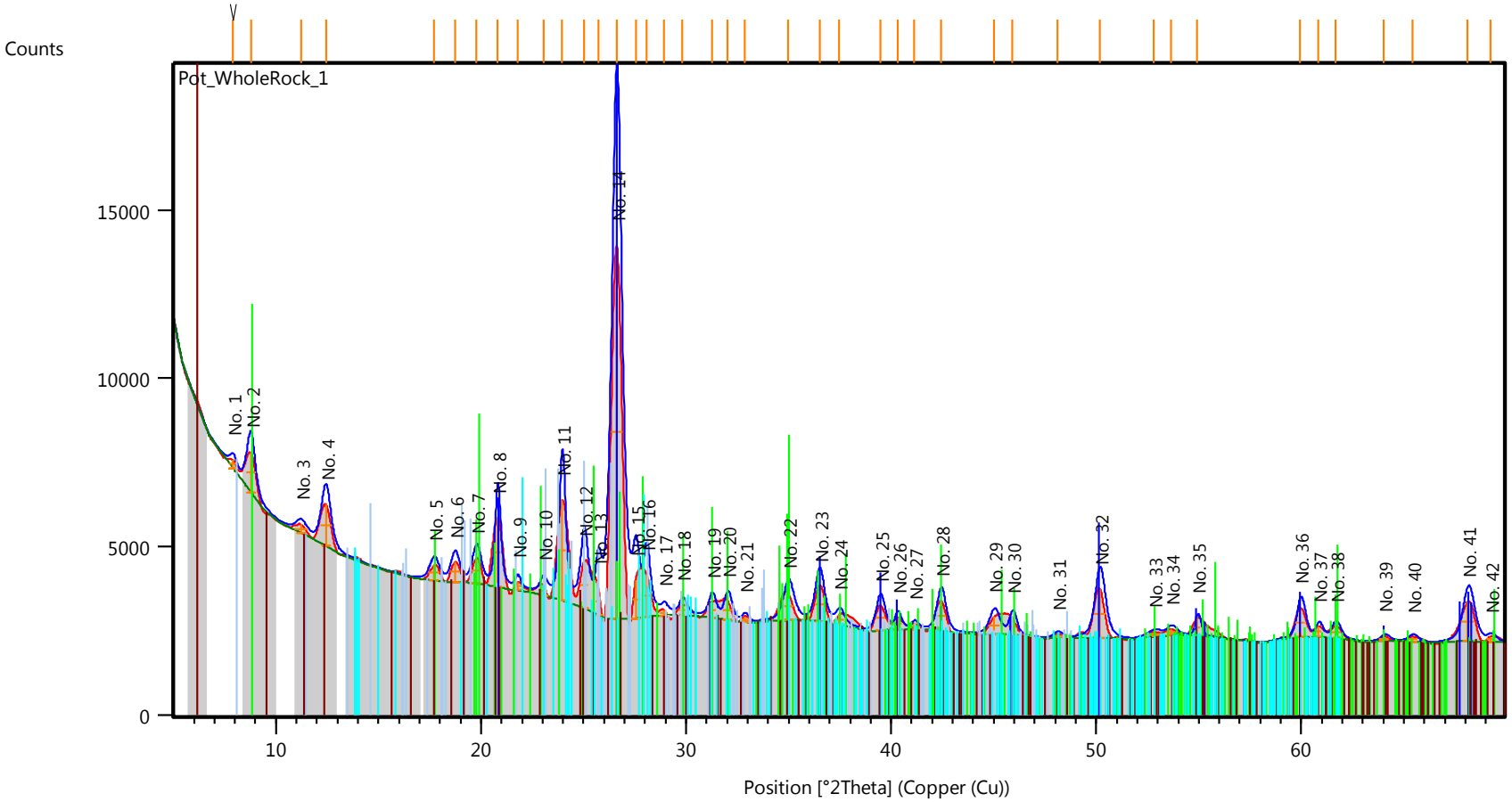

Pottsville Whole Rock PANalytical High Score Analysis

Parkwood Whole Rock XRD PANalytical High Score Analysis

Muscovite represents the 10 Å clay illite
Vermiculite represents the 14 Å clay Chlorite

Peak #	°2Theta	Intensity	d-Spacing [Å]	Rel. Int. [%]	High Score Prediction
1	**7.9066**	252.9	11.18225	2.28	N/A
2	**8.7801**	1202.62	10.07153	10.84	Muscovite
3	**11.2214**	242.77	7.8853	2.19	Vermiculite
4	**12.4395**	1231.73	7.11579	11.1	Vermiculite
5	**17.7182**	458.74	5.00591	4.14	Muscovite
6	**18.7329**	589.32	4.737	5.31	Vermiculite
7	**19.7817**	758.68	4.48814	6.84	Muscovite
8	**20.8163**	2062.86	4.26736	18.6	Quartz
9	**21.7789**	245.2	4.08087	2.21	Muscovite
10	**23.0358**	299.12	3.86098	2.7	Muscovite
11	**23.9581**	2975.76	3.7144	26.83	Muscovite
12	**25.0272**	1408.7	3.5581	12.7	Muscovite
13	**25.7211**	793.88	3.46365	7.16	Muscovite
14	**26.6119**	11092.69	3.34971	100	Quartz
15	**27.5487**	1141.4	3.23788	10.29	Muscovite
16	**28.0733**	1243.71	3.17856	11.21	Muscovite
17	**28.9213**	154.1	3.08726	1.39	Muscovite
18	**29.8328**	308.51	2.99498	2.78	Muscovite
19	**31.2601**	463.08	2.86142	4.17	Muscovite
20	**32.032**	558.43	2.7942	5.03	Muscovite
21	**32.8556**	163.51	2.72602	1.47	Vermiculite
22	**34.9819**	805.96	2.56504	7.27	Muscovite
23	**36.4981**	1068.91	2.46189	9.64	Quartz
24	**37.4737**	303.6	2.40001	2.74	Muscovite
25	**39.4552**	728	2.28393	6.56	Quartz
26	**40.3119**	344.03	2.23735	3.1	Muscovite
27	**41.1275**	152.72	2.19484	1.38	Muscovite
28	**42.4226**	896.74	2.13079	8.08	Quartz
29	**45.0137**	507.58	2.01397	4.58	Muscovite
30	**45.9095**	504.58	1.97674	4.55	Quartz
31	**48.0932**	126.62	1.89196	1.14	Muscovite
32	**50.1596**	1462.18	1.81876	13.18	Quartz
33	**52.822**	129.73	1.73319	1.17	Muscovite
34	**53.6487**	189.36	1.70842	1.71	Muscovite
35	**54.935**	526.92	1.67142	4.75	Quartz
36	**59.9515**	879.99	1.54301	7.93	Quartz
37	**60.8368**	321.19	1.52266	2.9	Muscovite
38	**61.6581**	366.74	1.50433	3.31	Muscovite
39	**64.0351**	143.24	1.45411	1.29	Muscovite
40	**65.4107**	151.18	1.42682	1.36	Muscovite
41	**68.1118**	1182.6	1.37667	10.66	Muscovite
42	**69.2263**	153.31	1.35721	1.38	Muscovite

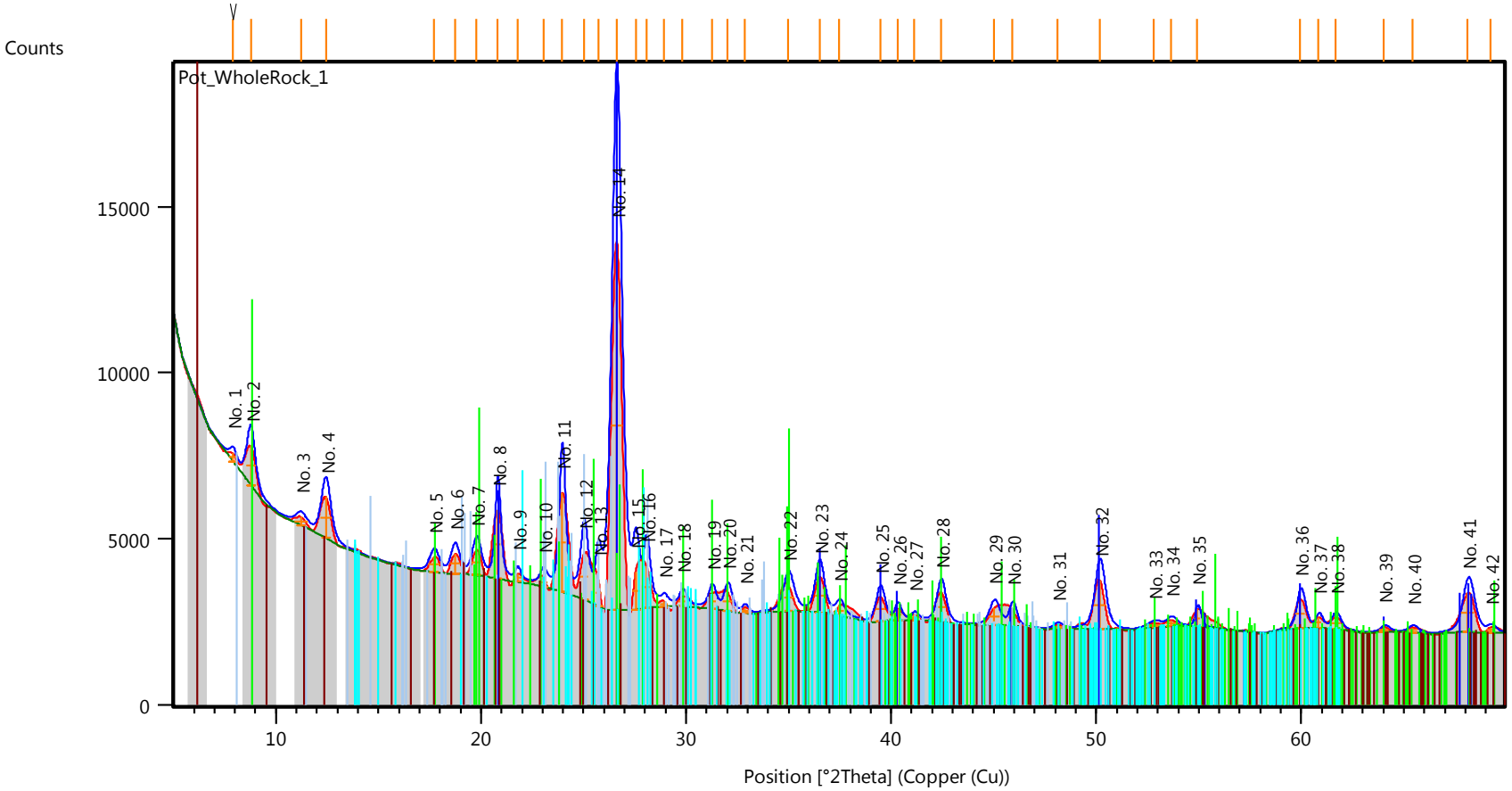

Parkwood Whole Rock PANalytical High Score Analysis

Clay Mineral Peak Data

Sample	Pos. [°2Th.]	d-spacing [Å]	Clay Mineral	Sample	Pos. [°2Th.]	d-spacing [Å]	Clay Mineral
Pottsville_Unaltered_Avg	6.1	14.38	**Fe-Chlorite**	**Parkwood_Unaltered_Avg**	6.1	14.40	**Fe-Chlorite**
	8.7	10.14	**Illite**		8.7	10.11	**Illite**
	12.3	7.18	**Fe-Ch/Kaolinite**		12.4	7.14	**Fe-Ch/Kaolinite**
	17.6	5.03	**Illite**		17.7	5.02	**Illite**
	18.7	4.74	**Fe-Chlorite**		18.7	4.74	**Fe-Chlorite**
	20.8	4.26	**Quartz**		23.0	3.90	**Quartz**
	25.0	3.56	**Fe-Chlorite**		25.9	3.44	**Fe-Chlorite**
	26.6	3.35	**Illite/Quartz**		28.5	3.14	**Illite/Quartz**
Pot_3hr	6.2	14.32	**Fe-Chlorite**	**PW_3hr**	6.1	14.44	**Fe-Chlorite**
	8.7	10.12	**Illite**		8.8	10.10	**Illite**
	12.4	7.17	**Fe-Ch/Kaolinite**		12.4	7.15	**Fe-Ch/Kaolinite**
	17.7	5.00	**Illite**		17.7	5.02	**Illite**
	18.7	4.74	**Fe-Chlorite**		18.7	4.74	**Fe-Chlorite**
	20.6	4.31	**Quartz**		20.7	4.29	**Quartz**
	25.1	3.55	**Fe-Chlorite**		25.1	3.54	**Fe-Chlorite**
	26.6	3.35	**Illite/Quartz**		26.6	3.35	**Illite/Quartz**
Pot_8hr	6.2	14.26	**Fe-Chlorite**	**PW_8hr**	6.1	14.56	**Fe-Chlorite**
	8.8	10.08	**Illite**		8.8	10.09	**Illite**
	12.4	7.15	**Fe-Ch/Kaolinite**		12.3	7.18	**Fe-Ch/Kaolinite**
	17.7	5.01	**Illite**		17.9	4.96	**Illite**
	18.8	4.72	**Fe-Chlorite**		18.8	4.72	**Fe-Chlorite**
	21.0	4.22	**Quartz**		20.7	4.29	**Quartz**
	25.1	3.54	**Fe-Chlorite**		25.1	3.54	**Fe-Chlorite**
	26.5	3.36	**Illite/Quartz**		26.6	3.35	**Illite/Quartz**
Pot_17hr	6.2	14.21	**Fe-Chlorite**	**PW_17hr**	6.0	14.80	**Fe-Chlorite**
	8.7	10.11	**Illite**		8.8	10.05	**Illite**
	12.4	7.15	**Fe-Ch/Kaolinite**		12.4	7.14	**Fe-Ch/Kaolinite**
	17.7	5.01	**Illite**		17.8	4.99	**Illite**
	18.8	4.72	**Fe-Chlorite**		18.7	4.75	**Fe-Chlorite**
	20.8	4.26	**Quartz**		20.8	4.27	**Quartz**
	25.1	3.55	**Fe-Chlorite**		25.1	3.54	**Fe-Chlorite**
	26.7	3.34	**Illite/Quartz**		26.6	3.35	**Illite/Quartz**
Pot_24hr	6.2	14.27	**Fe-Chlorite**	**PW_24hr**	6.1	14.58	**Fe-Chlorite**
	8.8	10.01	**Illite**		8.7	10.13	**Illite**
	12.4	7.17	**Fe-Ch/Kaolinite**		12.4	7.14	**Fe-Ch/Kaolinite**
	17.7	5.02	**Illite**		17.6	5.05	**Illite**
	18.7	4.74	**Fe-Chlorite**		18.6	4.78	**Fe-Chlorite**
	20.6	4.32	**Quartz**		20.9	4.25	**Quartz**
	25.1	3.55	**Fe-Chlorite**		25.2	3.54	**Fe-Chlorite**
	26.6	3.35	**Illite/Quartz**		26.6	3.35	**Illite/Quartz**
Pot_45hr	6.1	14.39	**Fe-Chlorite**	**PW_45hr**	6.1	14.53	**Fe-Chlorite**
	8.8	10.07	**Illite**		8.7	10.15	**Illite**
	12.4	7.16	**Fe-Ch/Kaolinite**		12.3	7.17	**Fe-Ch/Kaolinite**
	17.7	5.01	**Illite**		17.6	5.04	**Illite**
	18.8	4.73	**Fe-Chlorite**		18.6	4.76	**Fe-Chlorite**
	21.2	4.19	**Quartz**		20.7	4.29	**Quartz**
	25.0	3.56	**Fe-Chlorite**		25.1	3.55	**Fe-Chlorite**
	26.6	3.35	**Illite/Quartz**		26.6	3.35	**Illite/Quartz**
Pot_70hr	6.2	14.27	**Fe-Chlorite**	**PW_70hr**	6.2	14.30	**Fe-Chlorite**
	8.7	10.17	**Illite**		8.7	10.14	**Illite**
	12.3	7.19	**Fe-Ch/Kaolinite**		12.4	7.15	**Fe-Ch/Kaolinite**
	17.6	5.04	**Illite**		17.7	5.00	**Illite**
	18.7	4.75	**Fe-Chlorite**		18.7	4.74	**Fe-Chlorite**
	20.5	4.34	**Quartz**		20.8	4.28	**Quartz**
	25.0	3.56	**Fe-Chlorite**		25.1	3.54	**Fe-Chlorite**
	26.6	3.35	**Illite/Quartz**		26.6	3.35	**Illite/Quartz**

Appendix E - XRF Results

Sample	Time	Mass Sample (g)	wt % SiO2	wt % TiO2	wt % Al2O3	wt % Fe2O3	wt % MnO	wt% MgO	wt % CaO	wt % Na2O	wt % K2O	wt % P2O5	Total %	ppm Rb	ppm Sr	ppm Y	ppm Zr	ppm Nb
Pottsville	0	0.50	49.63	1.09	28.11	10.34	0.09	2.58	0.35	0.57	5.92	0.17	98.85	178.00	88.00	25.00	136.00	11.00
	3	0.43	51.04	1.09	25.97	10.52	0.09	2.48	1.06	0.89	6.09	0.16	99.40	190.97	81.02	18.52	133.10	12.73
	8	0.48	46.05	1.06	26.22	10.24	0.08	2.41	0.59	1.05	5.90	0.15	93.75	186.97	84.03	19.96	134.45	10.50
	17	0.47	50.10	1.03	27.66	10.60	0.10	2.49	1.12	0.99	5.77	0.17	100.03	177.59	81.40	22.20	127.91	12.68
	24	0.46	50.17	1.05	27.84	10.75	0.10	2.49	1.11	1.04	5.84	0.17	100.57	185.87	82.61	19.57	132.61	13.04
	45	0.48	50.40	1.03	28.17	10.62	0.08	2.46	1.03	1.15	5.81	0.17	100.91	182.39	80.71	22.01	131.03	11.53
	72	0.48	49.51	1.02	27.64	10.42	0.08	2.45	1.22	1.01	5.75	0.16	99.26	181.34	81.76	19.92	132.08	13.63
Parkwood	0	0.50	63.18	1.10	19.71	8.54	0.03	1.92	0.18	0.86	3.58	0.17	99.27	102.00	62.00	96.00	106.00	11.00
	3	0.49	60.69	1.06	20.94	9.16	0.03	2.10	0.81	1.16	3.89	0.17	100.00	115.54	57.26	96.11	103.27	8.18
	8	0.49	67.27	0.96	17.60	7.52	0.03	1.79	0.67	1.27	3.17	0.15	100.43	99.80	56.01	76.37	103.87	10.18
	17	0.49	59.44	1.05	20.65	9.33	0.03	2.12	0.71	1.25	3.92	0.17	98.66	113.50	61.35	91.00	102.25	9.20
	24	0.49	61.31	1.05	21.42	9.28	0.03	2.07	0.42	1.18	3.89	0.17	100.82	117.28	58.64	88.48	105.97	9.26
	45	0.48	69.33	1.12	19.75	8.40	0.00	1.96	0.80	1.34	3.52	0.18	106.38	105.26	57.89	88.42	110.53	9.47
	72	0.49	59.01	1.05	20.69	9.38	0.03	2.20	0.89	1.16	3.88	0.17	98.47	116.02	62.63	89.32	107.80	8.21

Appendix F - Batch Reaction Data

Batch Reaction Lab Data

Sample	Start Dat/Time	End Dat/Time	Hours	Vol Brine (mL)	Mass Sample	Mass CO2 (g)
Pot_Cube_Brine_NoCO2	11/8/11 18:00	11/15/11 15:00	165	18	2.599	~1.5
PW_Cube_Brine_NoCO2	11/15/11 16:00	11/22/11 18:00	167	18	2.491	~1.5
Pot_Cube_CO2	11/22/11 19:00	11/29/11 13:00	159	18	2.590	~1.5
PW_Cube_CO2	12/21/11 21:30	12/28/11 19:00	165.5	18	2.580	~1.5
Pot_Clay_CO2_8	12/11/11 14:00	12/11/11 22:00	8	18	0.407	~1.5
Pot_Clay_CO2_17	12/8/11 16:30	12/9/11 9:30	17	18	0.403	~1.5
Pot_Clay_CO2_24	12/9/11 13:00	12/10/11 13:00	24	18	0.409	~1.5
Pot_Clay_CO2_45	12/6/11 16:40	12/8/11 13:40	45	18	0.402	~1.5
Pot_Clay_CO2_70	11/5/11 15:45	11/8/11 13:45	70.25	18	0.408	~1.5
PW_Clay_CO2_3	1/13/12 14:30	1/13/12 17:30	3	18	0.407	~1.5
PW_Clay_CO2_8	1/15/12 14:45	1/15/12 22:45	8	18	0.408	~1.5
PW_Clay_CO2_17	1/10/12 14:30	1/11/12 19:30	17	18	0.410	~1.5
PW_Clay_CO2_24	1/9/12 12:00	1/10/12 12:00	24	18	0.405	~1.5
PW_Clay_CO2_45	12/16/11 20:30	12/17/11 17:30	45	18	0.404	~1.5
PW_Clay_CO2_70	12/11/11 22:40	12/14/11 20:40	70	18	0.408	~1.5
Pot_Na_Clay_CO2_3	2/19/12 13:50	2/19/12 16:50	3	18	0.548	~1.5
Pot_Na_Clay_CO2_8	2/24/12 13:00	2/24/12 21:00	8	18	0.550	~1.5
Pot_Na_Clay_CO2_17	2/4/12 19:00	2/5/12 12:00	17	18	0.550	~1.5
Pot_Na_Clay_CO2_24	2/5/12 13:30	2/6/12 13:30	24	18	0.550	~1.5
Pot_Na_Clay_CO2_45	2/1/12 15:00	2/3/12 12:00	45	18	0.544	~1.5
Pot_Na_Clay_CO2_70	2/10/12 20:00	2/13/12 18:00	70	18	0.550	~1.5
PW_Na_Clay_CO2_3	2/22/12 16:00	2/22/12 19:00	3	18	0.550	~1.5
PW_Na_Clay_CO2_8	2/20/12 11:40	2/20/12 7:40	8	18	0.551	~1.5
PW_Na_Clay_CO2_17	2/21/12 22:00	2/22/12 15:00	17	18	0.551	~1.5
PW_Na_Clay_CO2_24	2/20/12 21:00	2/21/12 21:00	24	18	0.551	~1.5
PW_Na_Clay_CO2_45	2/13/12 19:00	2/15/12 16:00	45	18	0.550	~1.5
PW_Na_Clay_CO2_70	2/15/12 17:00	2/18/12 15:00	70	18	0.550	~1.5

Appendix G - Atomic Absorbance Data

AA Detection of Silica in Brine

Silica			
Sample	**Corrected Peak Area**	**Concentration µg/L**	**Concentration Adjusted**
Blank w/ nitric	0.017	1	0.00019
Pot_3hr	0.107	7	0.00122
Pot_8hr	0.158	10	0.00180
Pot_17hr	0.201	14	0.00229
Pot_24hr	0.202	n/a	0.00230
Pot_45hr	0.164	11	0.00187
Pot_70hr	0.188	13	0.00214
PW_3hr	0.117	7	0.00133
PW_8hr	0.149	10	0.00170
PW_17hr	0.318	26	0.00363
PW_24hr	0.363	n/a	0.00414
PW_45hr	0.352	n/a	0.00401
PW_70hr	0.343	29	0.00391
Pot_Na_3hr	0.055	3	0.00063
Pot_Na_8hr	0.269	20	0.00307
Pot_Na_17hr	0.197	14	0.00225
Pot_Na_24hr	0.225	16	0.00257
Pot_Na_45hr	0.248	18	0.00283
Pot_Na_70hr	0.196	13	0.00223
PW_Na_3hr	0.106	6	0.00121
PW_Na_8hr	0.201	14	0.00229
PW_Na_17hr	0.359	32	0.00409
PW_Na_24hr	0.447	46	0.00510
PW_Na_45hr	0.448	n/a	0.00511
PW_Na_70hr	0.445	n/a	0.00507
Pot_Cube_NoCO2	0.104	6	0.00119
PW_Cube_NoCO2	0.21	15	0.00239
Pot_Cube_CO2	0.136	9	0.00155
PW_Cube_CO2	0.218	15	0.00249

AA Detection of Potassium in Brine

Potassium					
Sample	**Run 1**	**Run 2**	**Run 3**	**Average**	**Concentration Adjusted**
Brine	0.003	0.004	0.004	0.004	0.00005
Pot_3hr	0.270	0.269	0.273	0.271	0.00338
Pot_8hr	0.244	0.254	0.279	0.259	0.00324
Pot_17hr	0.304	0.305	0.297	0.302	0.00378
Pot_24hr	0.280	0.267	0.270	0.272	0.00340
Pot_45hr	0.413	0.415	0.422	0.417	0.00521
Pot_70hr	0.343	0.349	0.355	0.349	0.00436
PW_3hr	0.341	0.368	0.391	0.367	0.00458
PW_8hr	0.358	0.367	0.360	0.362	0.00452
PW_17hr	0.316	0.325	0.332	0.324	0.00405
PW_24hr	0.376	0.369	0.371	0.372	0.00465
PW_45hr	0.394	0.402	0.372	0.389	0.00487
PW_70hr	0.340	0.368	0.350	0.353	0.00441
Pot_Na_3hr	0.103	0.115	0.109	0.109	0.00136
Pot_Na_8hr	0.139	0.149	0.147	0.145	0.00181
Pot_Na_17hr	0.126	0.128	0.136	0.130	0.00163
Pot_Na_24hr	0.132	0.131	0.133	0.132	0.00165
Pot_Na_45hr	0.134	0.144	0.136	0.138	0.00173
Pot_Na_70hr	0.132	0.131	0.137	0.133	0.00167
PW_Na_3hr	0.142	0.141	0.153	0.145	0.00182
PW_Na_8hr	0.121	0.125	0.135	0.127	0.00159
PW_Na_17hr	0.155	0.151	0.154	0.153	0.00192
PW_Na_24hr	0.168	0.174	0.177	0.173	0.00216
PW_Na_45hr	0.152	0.148	0.150	0.150	0.00188
PW_Na_70hr	0.160	0.165	0.172	0.166	0.00207
Pot_Cube_NoCO2	0.137	0.143	0.135	0.138	0.00173
PW_Cube_NoCO2	0.142	0.152	0.149	0.148	0.00185
Pot_Cube_CO2	0.182	0.191	0.185	0.186	0.00233
PW_Cube_CO2	0.152	0.158	0.156	0.155	0.00194